Theses and Dissertations   Student Graduate Works

3-22-2019

Computational and Experimental Development of 2D Anisotropic Photonic Crystal Metamaterials

James A. Ethridge

Follow this and additional works at: https://scholar.afit.edu/etd

Part of the Materials Science and Engineering Commons, and the Physics Commons

**Computational and Experimental Development
of 2D Anisotropic Photonic Crystal
Metamaterials**

THESIS

James A. Ethridge

AFIT-ENP-MS-19-M-077

**DEPARTMENT OF THE AIR FORCE
AIR UNIVERSITY**

AIR FORCE INSTITUTE OF TECHNOLOGY

Wright-Patterson Air Force Base, Ohio

The views expressed in this document are those of the author and do not reflect the official policy or position of the United States Air Force, the United States Department of Defense or the United States Government. This material is declared a work of the U.S. Government and is not subject to copyright protection in the United States.

AFIT-ENP-MS-19-M-077

Computational and Experimental Development of 2D Anisotropic Photonic Crystal Metamaterials

THESIS

Presented to the Faculty

Department of Engineering Physics

Graduate School of Engineering and Management

Air Force Institute of Technology

Air University

Air Education and Training Command

in Partial Fulfillment of the Requirements for the

Degree of Master of Science in Applied Physics

James A. Ethridge, B.S.

March 21 2019

DISTRIBUTION STATEMENT A.

APPROVED FOR PUBLIC RELEASE; DISTRIBUTION UNLIMITED

Computational and Experimental Development of 2D Anisotropic Photonic Crystal
Metamaterials

THESIS

James A. Ethridge, B.S.

Committee Membership:

Dr. M. A. Marciniak
Chair

Lt Col S. D. Butler PhD
Member

Dr. M. J. Havrilla
Member

Dr. A. M. Sarangan
Member

Abstract

The future of optical devices involves manipulation of nanoscale structure in order to achieve full control over the properties of the device. In fields as diverse as directed energy, remote sensing, optical communications and optical computing, these devices promise to greatly improve performance and efficiency. To advance this further, novel samples that incorporate both photonic crystal (PhC) structure and metamaterial properties, known as PhC metamaterials, are proposed. These PhC metamaterials allow for complete control over the directionality of the light-matter interaction to serve in these new applications. To develop this technology, first, metamaterials with no PhC structure are fabricated using the technique of glancing angle deposition (GLAD) in the form of nanorod or nanohelical structures. These metamaterials are then characterized using Variable-Angle Spectral Ellipsometry (VASE) to extract their optical constants. Using these measured effective material parameters, a model for the corresponding metamaterial within a PhC structure was developed in COMSOL Multiphysics to calculate the photonic bandgap (PBG) of that structure. Results show that a material with a complete and large PBG can be achieved with these PhC metamaterials. Future measurements include that of the temperature dependence and polarimetric scatterometry of these PhC metamaterials.

Table of Contents

List of Tables

List of Figures

x

Computational and Experimental Development of 2D Anisotropic Photonic Crystal Metamaterials

I. Introduction

1.1   General Issue

Photonic crystals and metamaterials have each recently become critical areas of research in the field of optics, with each offering different opportunities and challenges. Photonic crystals have already been used to increase the speed of optical communication through photonic crystal fibers [1] [2] [3] [4], and many more applications are possible. Metamaterials offer huge advances in areas such as optical computing [5] and radar stealth [6] [7]. However, rarely have these two optical fields been combined in an effective way. This work attempts to combine these techniques to offer more customizability and more effectiveness in applications such as optical computing, optical communications, and directed energy. This offers incredible new opportunities, but the challenges involved also increase.

1.2   Relevant Research

The first research on anisotropic photonic crystals was done in the 1D case, i.e layered films [8]. In that case, it is not possible to achieve a complete optical bandgap (see chapter 2 for discussion), but different researchers were able to achieve a near complete bandgap, which results in the property of omnidirectional reflection [9]. These 1D materials are often easier to fabricate and analyze, but they are limited in customizability and bandgap size. More advanced tests of omnidirectional reflectors

came in [10].

After this 1D work, more research was performed on 2D anisotropic photonic crystals. 2D photonic crystals have a 2D periodic structure in a single plane and are often used as a waveguide. These studies often use computational techniques such as the plane wave expansion method [11], the transfer matrix method [12], or the Dirichlet-to-Neumann map method [13]. The first papers established that using anisotropic materials would indeed lead to larger bandgaps [14][15], using the plane wave expansion method. Next, simple photonic crystal structures with natural anisotropic materials were fabricated and tested. There have been tests of the square lattice using the transport matrix method [16], the square and triangular lattices using the Dirichlet-to-Neumann map method [17], and the triangular lattice using the finite difference time domain method [18] [19]. These materials can also be analyzed from a symmetry perspective [20] [21], which can be applied to any arbitrary lattice, and allows for computational simplification. Symmetry reduction techniques, such as adding defects, can also increase the size of the bandgap [22]. By 2013, the first tests of 3D anisotropic photonic crystals had begun [23], but the fabrication requirements were still prohibitive at that time. None of this research except [24] used metamaterials as the anisotropic component, and that was only in the 1D case.

Many different types of anisotropic metamaterials have been studied, such those using wire grid formulations [25] and those using split-ring resonators [26]. However, these types of anisotropic metamaterial structures were not used in this work, rather, structures based on nanorods or nanohelices were used. The unique nature of these anisotropic metamaterials has been studied in a few papers. Silver nanorods were optically characterized using ellipsometry in [27], chromium nanorods were characterized in [28], and titanium nanorods were characterized in [29]. Examples of applications that have been studied for these nanorod materials are ultracompact waveplates [30]

2

and antireflection coatings [31].

1.3   Research Objectives

In this thesis, the theory, design, and analysis of photonic crystal metamaterials will be explored. Specifically, the theories of anisotropic materials and photonic bandgaps are covered, with a focus on the plane wave expansion method. This research combines two rarely combined fabrication methods, glancing angle deposition and photolithography. This results in materials that exhibit a photonic bandgap. This research seeks to measure metamaterials experimentally using variable angle spectral ellipsometry, and calculate the photonic bandgaps using computational simulation. The computational simulation is done using COMSOL Multiphyics. These bandgaps will determine the capabilities of the materials and possibilities for applications. The fully customizable nature of these photonic metamaterials will allow for many varied applications.

1.4   Methodology

The first step was to use glancing angle deposition (GLAD) to create anisotropic metamaterials. Next, the optical constants of these anisotropic metamaterials without any photonic crystal structure were characterized. This characterization was done using variable angle spectral ellipsometry (VASE) in the infrared regime. Next, using the software COMSOL Multiphysics, a model was created for a photonic crystal metamaterial using the experimentally derived optical constants. The modeled structures were analyzed using the plane wave expansion method to determine the photonic bandgaps. Then, anisotropic metamaterials with a photonic crystal structure are fabricated using GLAD combined with interferometric photolithography to prove feasibility of using such samples in physical applications. Initial test designs

3

of the metamaterials are based on ease of fabrication. Materials such as vanadium oxide (V_yO_x), chromium (Cr), and germanium-antimony-tellurium (GST) were used to deposit the nanostructure which forms the metamaterials.

1.5 Limitations

When fabricating these nanostructured metamaterials, the resultant is not uniform due to fabrication tolerances. At this time, the resultant uncertainty from this non-uniformity is not characterized. Some of the base materials used in this work are metals, which in general have magnetic properties, but that is not considered in this work since a different and less efficient computational would need to be used in that case. The experimental method itself has a well-characterized error, fully derived in [32]. Thus it is possible to determine uncertainty in the optical constants from the ellipsometric measurements. However, the VASE system does not account for an incident circular polarization, which could impact the results for the nanostructured metamaterials that have a circular nature. Also, it is currently not possible to accurately propagate the experimental uncertainty into the computational simulation. More theoretical work needs to be done to ensure that the uncertainty would propagate correctly. When doing the computational simulations, the nonlinear solver needed to solve the planewave method sometimes fails to converge for absorptive materials, which is a known problem with the plane wave expansion method. The fabrication process itself is currently limited to certain periodic designs and base materials, but this may change in the future.

1.6 Overview

Chapter II provides the theoretical background to the other sections of the work. Chapter III contains the methodology for the fabrication, experimental analysis, and

4

computational analysis of the photonic metamaterial samples. Chapter IV describes and analyzes the results of these methods. Chapter V concludes the work by summarizing it and making recommendations for future research.

II. Theoretical Background

2.1 Chapter Overview

In this chapter, the basics of anisotropic materials and photonic crystals are discussed. Topics such as symmetry operations, the Bloch theorem, field decomposition, and the plane wave expansion method will be covered. A detailed understanding of the photonic bandgap and where it comes from will be achieved. An overview of relevant materials will also be provided. Relevant citations have been provided to supplement a given discussion or offer a resource for a more detailed development of a specific topic.

2.2 General Anisotropic Materials

The electromagnetic field's interaction with any material is governed by certain macroscopic properties, both its permittivity, ϵ, and its permeability, μ. For this section, assume no magnetic interaction, thus $\mu = \mu_0$. Note that the permittivity defines the dielectric properties of the material and may be complex in general. For isotropic materials, there is only one value for ϵ, but generally, the dielectric properties of every material can be represented by a dielectric tensor, which will be written

$$\overleftrightarrow{\epsilon} = \begin{bmatrix} \epsilon_{xx} & \epsilon_{xy} & \epsilon_{xz} \\ \epsilon_{yx} & \epsilon_{yy} & \epsilon_{yz} \\ \epsilon_{zx} & \epsilon_{zy} & \epsilon_{zz} \end{bmatrix}, \tag{1}$$

where x, y, z define an arbitrary rectangular coordinate system.

Theoretically, each of these directional permittivities may be different, which leads to a large number of variables in any material characterization. However, the number of variables can be reduced by applying symmetry to the material, with more

6

symmetry leading to a material with fewer variables to determine. There are several categories of anisotropic materials that are grouped by their symmetries, and two important categories are uniaxial and biaxial materials. Uniaxial materials have a single axis that governs the anisotropy, which is known as the optic axis of the material. Rotating around this axis does not change the behavior of the material, so this is a symmetry that reduces the number of variables to characterize. Assuming the optic axis is aligned with the z-axis, a general dielectric tensor for uniaxial tensors is

$$\overleftrightarrow{\epsilon} = \begin{bmatrix} \epsilon_t & 0 & 0 \\ 0 & \epsilon_t & 0 \\ 0 & 0 & \epsilon_z \end{bmatrix}, \tag{2}$$

where ϵ_t is in the directions perpendicular to optic axis, while ϵ_z is in the direction of the optic axis. Another convention uses ϵ_o instead of ϵ_t to represent the "ordinary" transmission which is not affected by the anisotropy, and uses ϵ_e instead of ϵ_z to represent the "extraordinary" transmission, which is affected by the anisotropy. In any case, using symmetry, there are now only two variables needed rather than nine needed in the general case to characterize the material.

The case of biaxial materials is more complicated than uniaxial materials. In that case, there are two special optical axes. This makes the symmetry operations much harder to visualize, as there is no obvious rotation symmetry like in the uniaxial case. Without that symmetry, the dielectric tensor becomes

$$\overleftrightarrow{\epsilon} = \begin{bmatrix} \epsilon_x & 0 & 0 \\ 0 & \epsilon_y & 0 \\ 0 & 0 & \epsilon_z \end{bmatrix}, \tag{3}$$

assuming that the chosen rectangular coordinate system aligns with these two optical

7

axes. So even in this more complicated case, the number of variables is reduced from nine to three. The power of symmetry is clear, so when a novel material is created, it becomes necessary to analyze its symmetries. The anisotropic materials covered in this work are fabricated through the process of glancing angle deposition (GLAD), which will be discussed in the next chapter, but these materials have a unique form, as shown in Figure 1.
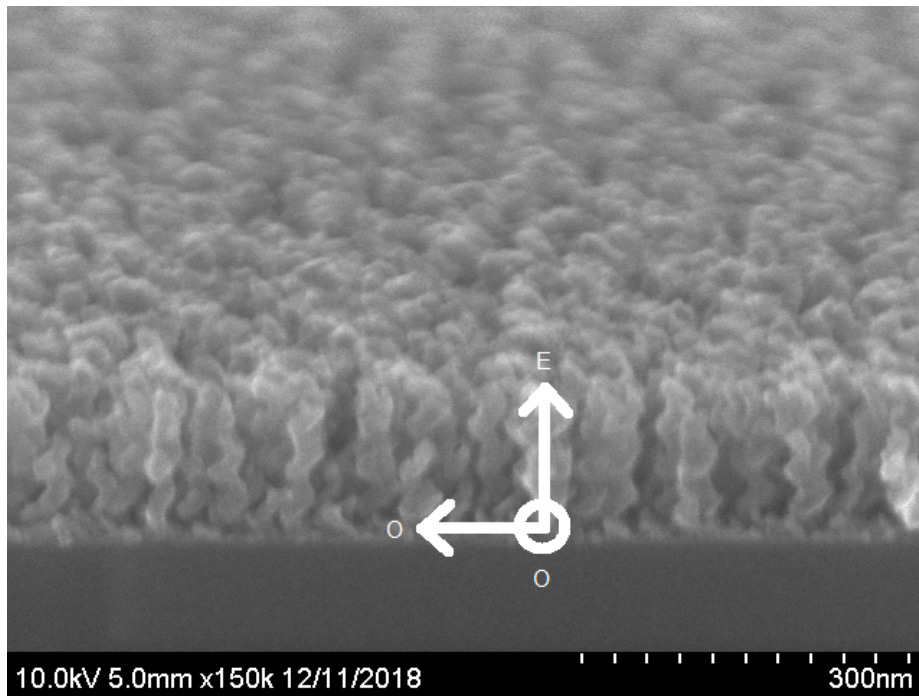
Figure 1. Scanning Electron Microscope (SEM) image of V_yO_x nanohelix metamaterial. Taken by Dr. Sarangan at the University of Dayton. Used with permission.

Since the nanohelicies are at a 90° angle with the plane, rotating around the axis of the nanorods is symmetrical, so the material should be uniaxial.

To analytically determine if it is actually uniaxial, the actual symmetry operations are needed. These can also be defined as transformations, each one defining a three by three transformation matrix $\overleftrightarrow{T}$. As an example, the transformation matrix for a 90° rotation around the z-axis, referred to as the 4_z operation, where the 4 comes

from $\frac{360}{90}$, would be

$$\overleftrightarrow{T_{4_z}} = \begin{bmatrix} 0 & 1 & 0 \\ -1 & 0 & 0 \\ 0 & 0 & 1 \end{bmatrix}. \tag{4}$$

When applying this transformation, the x'-axis now points in the direction of the y-axis, the y'-axis now points in the direction of the $-x$-axis, and the z'-axis is the same as the z-axis. These transformation matrices can be derived for any symmetry operation. There are general forms for each different type of symmetry operation, such as rotation, reflection, and inversion.

To determine what effect symmetries have on the dielectric tensor, Neumann's principle is used. For ϵ, the spatial Neumann's principle, which applies if the transformation is purely spatial, states

$$\overleftrightarrow{T} \cdot \overleftrightarrow{\epsilon} = \overleftrightarrow{\epsilon} \cdot \overleftrightarrow{T}. \tag{5}$$

And the spatial-temporal Neumann's principle, which applies if the transformation has a temporal element, states

$$\overleftrightarrow{T} \cdot \overleftrightarrow{\epsilon} = \overleftrightarrow{\epsilon}^T \cdot \overleftrightarrow{T}. \tag{6}$$

Thus there is an equation for each transformation, and applying the information from each transformation reduces the number of variables in the dielectric tensor. The symmetry operations of the material from Figure 1 can be derived under different assumptions but the same result is achieved in any case. If it is assumed that the nanohelicies are arranged in a square lattice, then the symmetry operations will be discrete, instead of continuous as they would be under different assumptions. With this assumption, there will be many symmetries present.

9

Note that this work will use the notation of the International Union of Crystallography (IUC). In every case, there is the identity operation, notated by 1. There is mirror symmetry in the x and y directions, along with the xy and $-xy$ directions. These symmetries are notated by m_x, m_y, m_{xy}, and $m_{\bar{x}y}$. There are several rotational symmetries with z as the axis of rotation, which are 180°, and ±90°. These are notated by 2_z and $\pm 4_z$. Thus there is a total of eight symmetry elements, $\{1, m_x, m_y, m_{xy}, m_{\bar{x}y}, 2_z, 4_z, -4_z\}$, which is the symmetry group $4mm$. Note that in this specific case, where magnetic interaction is ignored, it is possible to include time reversal symmetry. However, in this case, the form of the dielectric remains the same whether time reversal symmetry is included or not. It is not necessary to apply the transformation matrix of each of the eight symmetry operations, but rather just the generating elements which in this case are $\{4_z, m_x\}$. These are known as the generators because the other six elements of the symmetry group can be found by multiplying the generators together or with themselves. For example, $4_z \cdot 4_z = 2_z$, since two 90° rotations equal one 180° rotation. So only the transformation matrices of 4_z and m_x are needed, and the 4_z was already shown as an example. The m_x transformation matrix is

$$\overleftrightarrow{T_{m_x}} = \begin{bmatrix} -1 & 0 & 0 \\ 0 & 1 & 0 \\ 0 & 0 & 1 \end{bmatrix}. \tag{7}$$

Now applying the spatial Neumann's principle will give the form of the dielectric

tensor. First applying the 4_z transformation,

$$\overleftrightarrow{T_{4_z}} \cdot \overleftrightarrow{\epsilon} \;=\; \overleftrightarrow{\epsilon} \cdot \overleftrightarrow{T_{4_z}} \tag{8}$$

$$\begin{bmatrix} 0 & 1 & 0 \\ -1 & 0 & 0 \\ 0 & 0 & 1 \end{bmatrix} \cdot \begin{bmatrix} \epsilon_{xx} & \epsilon_{xy} & \epsilon_{xz} \\ \epsilon_{yx} & \epsilon_{yy} & \epsilon_{yz} \\ \epsilon_{zx} & \epsilon_{zy} & \epsilon_{zz} \end{bmatrix} = \begin{bmatrix} \epsilon_{xx} & \epsilon_{xy} & \epsilon_{xz} \\ \epsilon_{yx} & \epsilon_{yy} & \epsilon_{yz} \\ \epsilon_{zx} & \epsilon_{zy} & \epsilon_{zz} \end{bmatrix} \cdot \begin{bmatrix} 0 & 1 & 0 \\ -1 & 0 & 0 \\ 0 & 0 & 1 \end{bmatrix} \tag{9}$$

$$\begin{bmatrix} \epsilon_{yx} & \epsilon_{yy} & \epsilon_{yz} \\ -\epsilon_{xx} & -\epsilon_{xy} & -\epsilon_{xz} \\ \epsilon_{zx} & \epsilon_{zy} & \epsilon_{zz} \end{bmatrix} = \begin{bmatrix} -\epsilon_{xy} & \epsilon_{xx} & \epsilon_{xz} \\ -\epsilon_{yy} & \epsilon_{yx} & \epsilon_{yz} \\ -\epsilon_{zy} & \epsilon_{zx} & \epsilon_{zz} \end{bmatrix} \tag{10}$$

This implies that $\epsilon_{yx} = -\epsilon_{xy}, \epsilon_{xx} = \epsilon_{yy}, -\epsilon_{xz} = \epsilon_{yz} = \epsilon_{xz}$, and $-\epsilon_{zy} = \epsilon_{zx} = \epsilon_{zy}$. The last two conditions further imply that $\epsilon_{xz}, \epsilon_{yz}, \epsilon_{zx}, \epsilon_{zy} = 0$. Thus the updated dielectric tensor is

$$\overleftrightarrow{\epsilon} = \begin{bmatrix} \epsilon_{xx} & \epsilon_{xy} & 0 \\ -\epsilon_{xy} & \epsilon_{xx} & 0 \\ 0 & 0 & \epsilon_{zz} \end{bmatrix}, \tag{11}$$

Now apply the spatial Neumann's principle with the m_x transformation.

$$\overleftrightarrow{T_{m_x}} \cdot \overleftrightarrow{\epsilon} \;=\; \overleftrightarrow{\epsilon} \cdot \overleftrightarrow{T_{m_x}} \tag{12}$$

$$\begin{bmatrix} -1 & 0 & 0 \\ 0 & 1 & 0 \\ 0 & 0 & 1 \end{bmatrix} \cdot \begin{bmatrix} \epsilon_{xx} & \epsilon_{xy} & 0 \\ -\epsilon_{xy} & \epsilon_{xx} & 0 \\ 0 & 0 & \epsilon_{zz} \end{bmatrix} = \begin{bmatrix} \epsilon_{xx} & \epsilon_{xy} & 0 \\ -\epsilon_{xy} & \epsilon_{xx} & 0 \\ 0 & 0 & \epsilon_{zz} \end{bmatrix} \cdot \begin{bmatrix} -1 & 0 & 0 \\ 0 & 1 & 0 \\ 0 & 0 & 1 \end{bmatrix} \tag{13}$$

$$\begin{bmatrix} -\epsilon_{xx} & -\epsilon_{xy} & 0 \\ -\epsilon_{xy} & \epsilon_{xx} & 0 \\ 0 & 0 & \epsilon_{zz} \end{bmatrix} = \begin{bmatrix} -\epsilon_{xx} & \epsilon_{xy} & 0 \\ \epsilon_{xy} & \epsilon_{xx} & 0 \\ 0 & 0 & \epsilon_{zz} \end{bmatrix} \tag{14}$$

This implies that $-\epsilon_{xy} = \epsilon_{xy}$, which further implies that $\epsilon_{xy} = 0$. The updated

11

dielectric tensor is

$$\overleftrightarrow{\epsilon} = \begin{bmatrix} \epsilon_{xx} & 0 & 0 \\ 0 & \epsilon_{xx} & 0 \\ 0 & 0 & \epsilon_{zz} \end{bmatrix}. \tag{15}$$

Thus it can be seen that nanohelical material has the form of a uniaxial material. Also note that using the tables from [33], it is possible look up the symmetry group that contains the operations and see immediately what the form of the dielectric tensor would be.

In any case, it has been shown that when there is a substrate plane, the nanohelix material does act as a uniaxial material. So theoretically, there are only two variables needed to characterize the optical properties of the material. Of course, these dielectric values vary with wavelength, so a wide spectral band method should be used for that important information. One experimental method for determining these dielectric values will be discussed in the next chapter. There are other metamaterials that can be created using glancing angle deposition, such as tilted nanorod structures. The symmetry calculations for these metamaterials will not be worked out in this work, due to similarity to the already shown derivation.

2.3   Basics of Bandgaps

In this work, there is more to understand than just anisotropic materials, there is also photonic crystal behavior to understand. Some terminology from solid state physics is necessary to understand photonic crystals and the photonic bandgaps. The lattice is the repeating pattern of the material that has translational symmetry. A region of the lattice that can be translated along the basis vectors to give the entire lattice is known as a unit cell. The smallest possible unit cell is known as the primitive unit cell. It is always possible to find a primitive unit cell using the technique known as

the Wigner-Seitz construction. Another important construct is the reciprocal lattice, which can be generated from the basis vectors of the direct lattice. Theoretically, the reciprocal lattice is a 3D mapping of the propagation vectors resulting from a plane wave decomposition of the direct lattice. It is also possible to construct a primitive unit cell for the reciprocal lattice, which is known as the first Brillouin zone.

Photonic crystals themselves are periodic optical micro or nanostructures that exhibit unique effects due to their periodicity. This periodicity, which is a translational symmetry, could be analyzed using the same techniques as in the last section. However, since light propagating in these structures has theoretical similarity to how electrons interact with bulk crystals, which has been studied in the field of solid state physics, a different development will be followed. One well known theorem from solid state physics that elucidates the situation is the Bloch theorem. This applies for both traditional solid state physics systems, as well the photonic crystal systems of this work. The theorem states the energy eigenstates for the system can be written as Bloch waves, which are of the form $\psi(r) = e^{ik \cdot r} u(r)$, where $u(r)$ is a function with the same periodicity as the system and k is the crystal wave vector, which is directly related to the crystal momentum. The crystal momentum is defined as $\hbar k$, where $\hbar$ is the reduced Planck constant. Note that the crystal momentum is not a true momentum, but acts like a free particle momentum in many situations. The proof of the Bloch theorem will not be stated here, as it can be found in any solid state physics textbook, such as [34].

The consequences of this seemingly simple theorem are profound. One of them is that the first Brillouin zone is the only one that matters, or in other words, the first Brillouin zone contains all the information about the wave solutions. In a 2D photonic crystal, finding the Brillouin zone is much more complicated, but is not impossible, see [35] for more. When there is a simple system, it is possible to analytically determine

13

the bandgap for this first Brillouin zone. One such system is the Kronig-Penney model. Note that development from [34] is followed in this work. This system has a potential depicted in Figure 2, modified from [34].
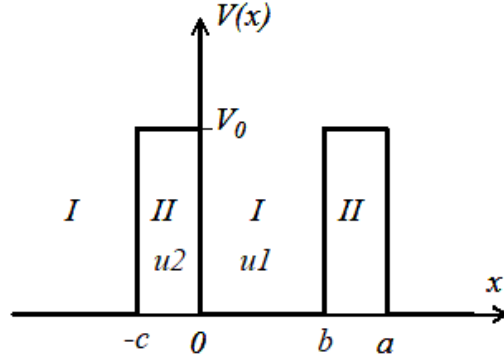
Figure 2. Potential for the Kronig-Penny model. There are two regions, one where $V(x) = 0$, and one where $V(x) = V_0$. The periodicity of a unit cell is a, or $b + c$.

This is a basic 1D model of a potential, but it reveals much about more complicated systems. To solve, Schrodinger's equation is set up in each of the different regions in one period. For region $V(x) = 0$, $0 < x < b$,

$$\frac{d^2\psi}{dx^2} + \frac{2m}{\hbar^2}E\psi(x) = 0. \tag{16}$$

For region $V(x) = V_0$, $-c < x < 0$,

$$\frac{d^2\psi}{dx^2} + \frac{2m}{\hbar^2}[E - V_0]\psi(x) = 0. \tag{17}$$

Substituting the known form of the solution from the Bloch theorem, $\psi(x) = e^{ikx}u(x)$, there are two new equations which are now in terms of $u(x)$,

$$\frac{d^2u_1}{dx^2} + 2ik\frac{du_1}{dx} - (k^2 - \alpha^2)u_1(x) = 0, \tag{18}$$

14

$$\frac{d^2 u_2}{dx^2} + 2ik\frac{du_2}{dx} - (k^2 - \beta^2)u_2(x) = 0. \tag{19}$$

where $\alpha = 2mE/\hbar^2$, $\beta = 2m(E - V_0)/\hbar^2$, and u_1 and u_2 are the parts of $u(x)$ defined over all the intervals in the potential diagram. These are both linear second order differential equations, which can be solved. This will give an equation for $u_1(x)$ and an equation for $u_2(x)$, each with two arbitrary constants. To solve for these constants, the continuity condition of the wavefunction and the derivative of the wavefunction is applied. So there is a total of four equations and four unknowns, which can be solved. The result is, for $E > V_0$,

$$-\frac{\alpha^2 + \beta^2}{2\alpha\beta} \sin(\alpha b) \sin(\beta c) + \cos(\alpha b) \cos(\beta c) = \cos(ka). \tag{20}$$

In the other case, where $0 < E < V_0$, and making the substitution $\beta = i\gamma$,

$$\frac{\gamma^2 - \alpha^2}{2\alpha\gamma} \sin(\alpha b) \sin(\gamma c) + \cos(\alpha b) \cos(\gamma c) = \cos(ka), \tag{21}$$

where in both cases $a = b + c$. The key now is to realize $\cos(ka)$ is restricted to values on the interval $[-1, 1]$. This is because k and a are both real. It is obvious that a is real, since it is just the periodicity of the system, but k is real since an imaginary k leads to problems in the Bloch theorem. If $k = k_r + ik_i$, then $\psi = e^{i(k_r + ik_i)x}u(x) = e^{ik_r x}e^{-k_i x}u(x)$, which always has a real exponential factor, which will diverge at positive or negative infinity depending on the sign of k_i. Divergent wavefunctions are not allowed, so the real exponential factor must be eliminated, so k must be real.

Thus $\cos(ka)$ is restricted to $[-1, 1]$, but the left side of each equation is not so restricted. There are values of E, which is related to α and β, that will lead to the left side evaluating to a value outside of the interval $[-1, 1]$. These values of E are

15

forbidden, since they lead to a non-physical wavefunction. Therefore, these are the energies that make the bandgap, where no quantum states can exist. It is simple now to plot each equation as a function of k, which gives the well-known form of a band structure diagram. Thus the bandgap directly arises from the periodicity of the system, since it was solving for u_1 and u_2 that allowed the determination of the bandgap.

2.4 Photonic Crystal Bandgaps

The above is a quantum mechanical derivation, but it is related to the electromagnetic formulation that is used for photonic crystals. Instead of solving Schrodinger's equation, the goal is to solve Maxwell's equations. To demonstrate the similar form, make the assumptions of a linear, lossless medium, with $\mu = \mu_0$, and frequency independent dielectric constants, following [36]. It should be noted that some of the materials considered in this work are metals, and metals in general have magnetic properties, where $\mu \neq \mu_0$. That is not considered in this work, since completely different computational methods must be used which are much less efficient. Then Maxwell's equations become

$$\nabla \cdot \mathbf{H}(\mathbf{r}, t) = 0 \tag{22}$$

$$\nabla \cdot [\epsilon(\mathbf{r})\mathbf{E}(\mathbf{r}, t)] = 0 \tag{23}$$

$$\nabla \times \mathbf{E}(\mathbf{r}, t) + \mu_0 \frac{\partial \mathbf{H}(\mathbf{r}, t)}{\partial t} = 0 \tag{24}$$

$$\nabla \times \mathbf{H}(\mathbf{r}, t) - \epsilon_0 \epsilon(\mathbf{r}) \frac{\partial \mathbf{E}(\mathbf{r}, t)}{\partial t} = 0. \tag{25}$$

Equations (22) and (23) are known as the divergence equations, while equations (24) and (25) are the curl equations. Now it is common to represent the fields $\mathbf{E}(\mathbf{r}, t)$ and $\mathbf{E}(\mathbf{r}, t)$ in the frequency domain, so $\mathbf{E}(\mathbf{r}, t) = \mathbf{E}(\mathbf{r})e^{-i\omega t}$ and $\mathbf{H}(\mathbf{r}, t) = \mathbf{H}(\mathbf{r})e^{-i\omega t}$. Then

16

the divergence equations imply that the fields are built of transverse electromagnetic waves. The curl equations become

$$\nabla \times \mathbf{E}(\mathbf{r}) - i\omega\mu_0\mathbf{H}(\mathbf{r}) = 0 \tag{26}$$

$$\nabla \times \mathbf{H}(\mathbf{r},t) + i\omega\epsilon_0\epsilon(\mathbf{r})\mathbf{E}(\mathbf{r}) = 0. \tag{27}$$

To get the desired equation for one field only, divide Eq. (27) by $\epsilon(\mathbf{r})$ and take the curl. Then use Eq. (26) to eliminate $\mathbf{E}(\mathbf{r})$, leaving

$$\nabla \times \left(\frac{1}{\epsilon(\mathbf{r})} \nabla \times \mathbf{H}(\mathbf{r}) \right) = \left(\frac{\omega}{c} \right)^2 \mathbf{H}(\mathbf{r}). \tag{28}$$

In this equation, c is the speed of light, which is equal to $\sqrt{\epsilon_0\mu_0}$. This is the defining equation of a photonic crystal system, known as the master equation. This is an ordinary eigenvalue equation, with two operators, the curl operator $\nabla\times$ and the dielectric constant $\epsilon(\mathbf{r})$. The reason $\mathbf{H}(\mathbf{r})$ is used is that $\mathbf{E}(\mathbf{r})$ would result in a more complicated eigenproblem, since there would be operators on both sides. After determining $\mathbf{H}(\mathbf{r})$, it is simple to determine $\mathbf{E}(\mathbf{r})$ using Eq. (27).

Now consider Eq. (28) in the 1D case, similar to Kronig-Penney model. Then Eq. (28) becomes

$$\frac{d^2\mathbf{H}(x)}{dx^2} - \epsilon(x)\left(\frac{\omega}{c} \right)^2 \mathbf{H}(x) = 0. \tag{29}$$

This is very similar to the Schrodinger's equation that was used for the Kronig-Penny model, Eq. (16) and (17). The Bloch theorem could be used in a similar way to find solutions, if the system is simple enough. The dielectric constant acts like the potential did in the last section. Thus, the photonic bandgap is a direct result of the changing dielectric constant between regions of the photonic crystal. If the difference in dielectric constant between regions increases, then a larger photonic bandgap will

17

be possible. Also, for photonic band gaps, instead of regions of energy with no allowed quantum states, it is regions in frequency that do not allow propagation of electromagnetic waves. If there is a region that satisfies that for any incident polarization, it is a called a complete photonic bandgap. Sometimes, especially in 1D photonic crystals, it is not possible to achieve a complete photonic bandgap, but it is possible to create a frequency region where none of the allowed propagation states can couple to any possible incident propagating wave. This is referred to as an omnidirectional reflector (ODR) region [36].

Bandgaps are generally categorized not by their size in frequency, but rather by their gap-midgap ratio, which is defined as

$$R_g = \frac{\Delta\omega}{\omega_m}, \tag{30}$$

where $\Delta\omega$ is the size of the bandgap in frequency and ω_m is the midpoint of the bandgap. This gap-midgap ratio is often used as the figure of merit for different photonic crystal designs and can be used as the parameter to maximize in optimization schemes [37].

Again starting from Maxwell's equations, as above, and assuming a plane wave incident on the material, it is possible to decompose the electric field into transverse electric (TE) and transverse magnetic (TM) components. This is important for 2D photonic crystals, as it greatly reduces the complexity of the problem. In essence, the bandgap can be separately calculated for the TE and TM fields, and then the actual bandgap would be the where these two bandgaps overlap. However, for systems that are not as well-defined as the Kronig-Penny model or a corresponding simple electromagnetic system, new techniques are needed.

18

2.5 Computational Methods for Photonic Crystal Bandgaps

Analytic methods are useful for understanding the problem in more detail, however more complicated cases require a computational solution. One effective computational method specifically for finding the size and locations of the bandgaps is called the plane wave expansion method, and it is discussed in detail in references such as [36], [38]. Understanding the basic step of the plane wave expansion method is helpful in the results of this work, so a simplified derivation will be given. The first step is, as usual, to apply the Bloch theorem to get the form of the solutions. Thus $\mathbf{H}(\mathbf{r}) = \mathbf{u_k}(\mathbf{r})e^{i\mathbf{k}\cdot\mathbf{r}}$. Plugging this into the master equation, Eq. 28, gives a complicated expression for $\mathbf{u_k}(\mathbf{r})$ that cannot generally be analytically solved. To get an approximate solution, expand $\mathbf{u_k}(\mathbf{r})$ in terms of a Fourier series over the vectors $\mathbf{G}$, which are the reciprocal lattice vectors. The coefficients of the amplitudes of plane waves are summed together to give the full field, $\mathbf{H}(\mathbf{r})$, which is what gives the name, plane wave expansion method. By the definition of Fourier series, theoretically, an infinite number of plane waves would be required to fully represent the field, but practically there is always some cutoff. Convergence analysis is often performed to make sure the cutoff is not too low. If the fast Fourier transform is used to find the coefficients, then it is possible to include thousands of plane waves and still have a short time demand. The plane wave expansion is especially simple to apply for 1D cases, so it almost always used in those cases.

The plane wave expansion method can also be applied for more the complicated systems in this work. It can be applied in 2D, simply by expanding each component of the field separately. It can be applied for anisotropic materials, which means the permittivity must be treated as tensor, so each permittivity value must be expanded separately. Thus there is a significant increase in the number of operations in going from a simple 1D case to an anisotropic 2D case. The complexity increases even more

19

when the permittivity is treated as wavelength dependent. Other methods could be used to calculate the photonic band gap, such as the transfer matrix method [12], the finite difference time domain method [39], and the finite element method [40]. Most of these methods require larger computational resources, so the plane wave expansion is the most commonly used. Other methods could be used in the future to verify the results of this work.

2.6 Materials Literature Review

In this section, previous research on each base material examined in this work is presented, and the utilization of previous research on GLAD fabricated anisotropic metamaterials is discussed. One of the materials used in this work is vanadium oxide (V_yO_x). It is only recently starting to be used for optical applications, so the previous research on optical characterization is lacking. There is one study [41] that determined the reflectance and transmittance of V_yO_x in its different states. Figure 3 shows some of these results, modified from [41].
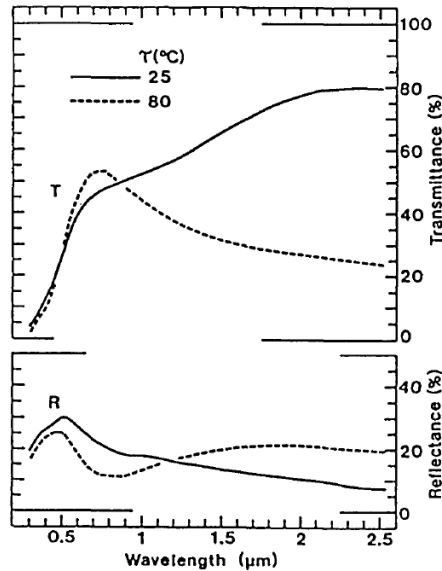
Figure 3. Transmission and Reflection of V_yO_x thin film.

In this work, all data was obtained at room temperature, so only the 25° case is relevant. Another material that is covered is germanium-antimony-tellurium (GST). This material has similar temperature dependence to V_yO_x, but it has been studied in more detail. One study on the optical properties of GST had results shown in Figure 4, modified from [42].

Refractive Index & Extinction Coefficient of Ge₂Sb₂Te₅
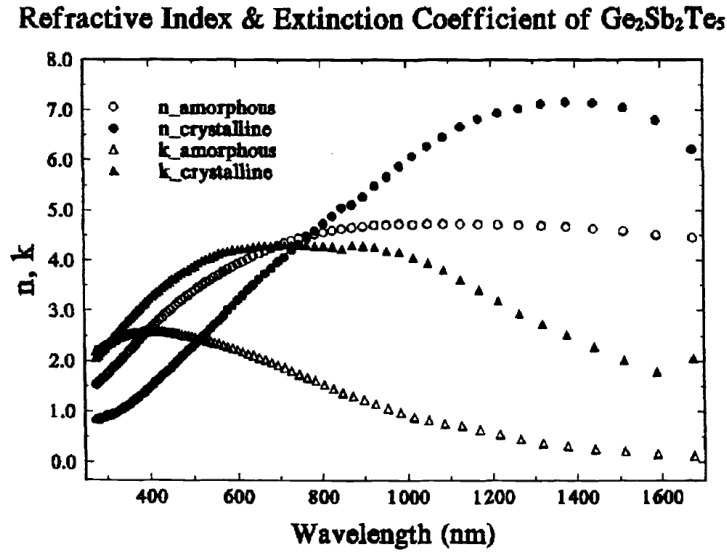
Figure 4. Optical Constants of GST thin film.

For room temperature GST, it is in the amorphous state. Again, all the data in this work was obtained at room temperature, so only the amorphous case is relevant for this work. Both GST and V_yO_x will be used in this work as base materials for the GLAD process. A material that used in previous GLAD work and in this work is chromium (Cr). This material has been studied much more extensively than GST or V_yO_x. There have been studies of thin films of Cr using ellipsometry [43]. There has also been studies of GLAD deposited nanorods in the visible using ellipsometry [28]. Figure 5 shows a scanning electron microscope (SEM) image of the Cr nanorod metamaterial and the sample axis orientation and Figure 6 shows some of these results in the visible, both modified from [28].

21

Figure 5. SEM image of Cr nanorod metamaterial.

Figure 6. Optical constants of Cr nanorod metamaterial and bulk Cr optical constants.

Figure 6 also shows the bulk optical constants from [44]. From the figures, it can

22

seen that the Cr nanorod metamaterial is birefringent, or in other words, there is a difference between the optical constants in different directions. It can also be seen that the GLAD metamaterial has very different properties than the bulk material. The last material used in previous work is silver (Ag). The bulk optical constants were characterized in [45], and GLAD deposited nanorod samples were measured using ellipsometry in [27]. Figure 7 shows an SEM image of Ag nanorod metamaterial and sample axis orientation and Figure 8 shows some of these results in the infrared, both modified from [27].
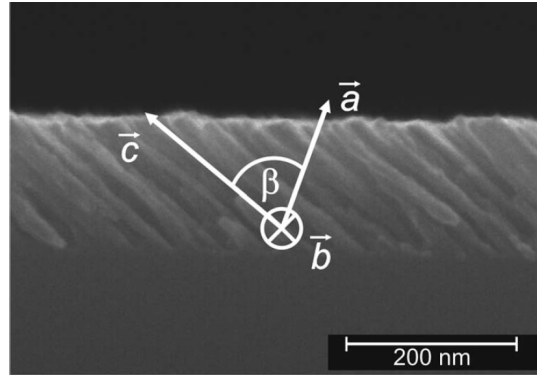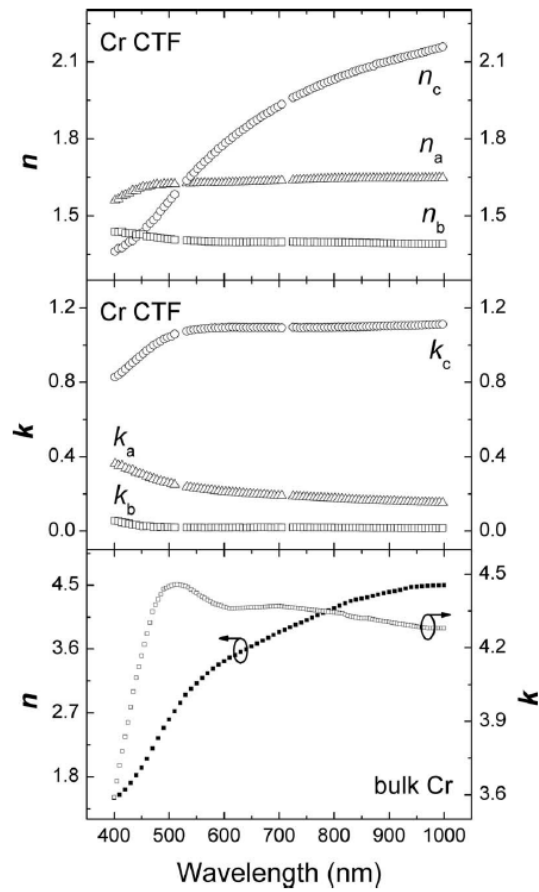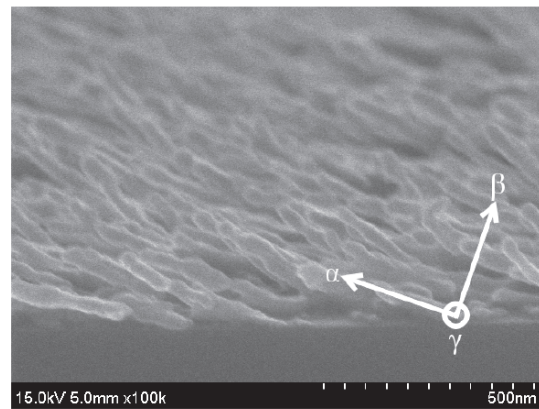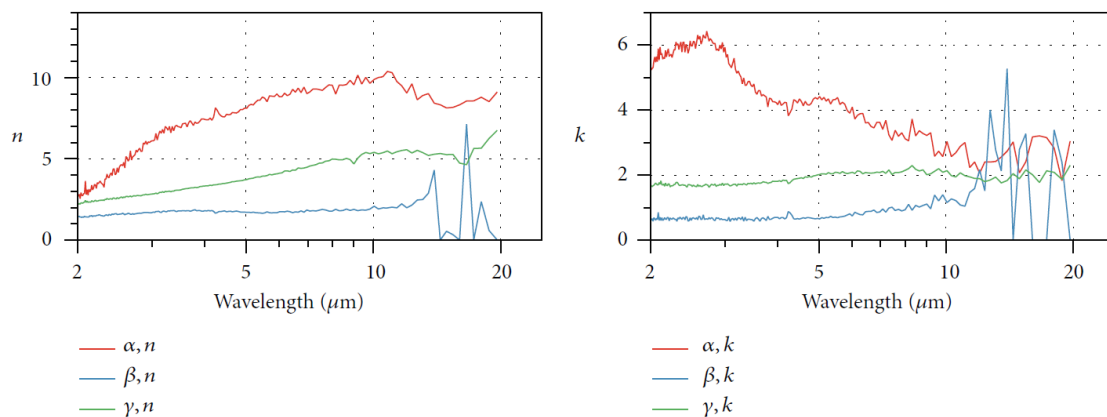

Figure 7. SEM image of Ag nanorod metamaterial.

Figure 8. Optical constants of Ag nanorod metamaterial.

23

From Figure 8, it can be seen that there is a large difference between the optical properties in different directions, but there are also high k values, which correspond to losses. The birefringence of a material is defined as the difference in refractive index along the different directions. Thus, in this case, the approximate maximum birefringence is about 8. In most solid state crystals, the birefringence is on the order of 0.1 [46]. The maximum birefringence that has been observed in a natural material, in the IR regime, is approximately 2 [47]. Thus, the much larger than typical birefringence for the Ag nanorods makes this an attractive option for achieving a complete photonic bandgap. Note that in previous ellipsometric characterizations of GLAD metamaterials, the optical constants were presented without an error estimation. That shortcoming will be addressed in this work.

2.7 Uniqueness of Current Work

Previous research has used the plane wave expansion method to create relationships between the permittivity or index of refraction and the known geometric properties of the material [14]. These are useful in predicting the bandgap for known geometries and materials. However, this work is different from that previous work, because the refractive index of the material itself was not a function of frequency. In other words, the materials were dispersionless. In this work, the materials were not assumed to be dispersionless, so the results from previous work cannot be directly used. Another difference in this work is it does not use natural anisotropic materials, in which the anisotropy cannot be modified as part of the design, but rather designed metamaterials for which the anisotropy can be completely controlled. This allows for more design options and synergy between the anisotropy and photonic crystal structure, but it does further imply that the results of previous work cannot be directly applied. The characterization will be discussed in detail in the next chapter.

Another question might arise as to what advantages anisotropy brings to 2D photonic crystals, since it leads to more difficult analysis. One reason is that anisotropy is a more advanced version of the well-known technique of symmetry breaking which works by introducing defects or impurities into the system. Symmetry breaking is important because less symmetry, while leading a more complex problem, is actually the key to reducing degeneracies that lead to smaller bandgaps. As a example, recall that the material bandgap for a 2D photonic bandgap can be thought of as the overlap of the TE and TM bandgaps. The anisotropic nature will affect either the TE or TM fields more than the other, which would allow for tuning of these two bandgaps to better line up and produce a larger complete bandgap. There are many ways that symmetry reduction can be beneficial to the properties of the material.

2.8   Summary

In summary, the theory of symmetry operations and their relationship to the dielectric tensor was established. Next, the theory of the photonic bandgap was established, first by looking at the solid state theory, then at the electromagnetic formulation. After that, the computational method for solving for photonic bandgaps was covered. Finally, the base materials used in this work were discussed. Now that the theory is understood, next is the methodology of the work.

III. Methodology

3.1 Chapter Overview

In this chapter, the basics of the different techniques involved in this work are covered. Firstly, the fabrication methods are covered, which are photolithography, interferometric lithography, and glancing angle deposition (GLAD). The fabrication was done in collaboration with Dr. Andrew Sarangan at the University of Dayton. Next, the experimental method is covered, which is variable angle spectral ellipsometry (VASE). The VASE apparatus was used at the compliments of the Materials and Manufacturing Directorate of the Air Force Research Laboratory. Lastly, the computational method is covered, which is a plane wave expansion eigenvalue analysis performed in COMSOL Multiphysics. Relevant citations have been provided to supplement a given discussion or offer a resource for a more detailed development of a specific topic.

3.2 Photolithography

Photolithography is a technique used in the creation of microelectronics, and more recently, of photonic crystals. Its goal is to pattern a substrate or a thin film. The first step in photolithography is to create an opaque, geometric mask with the pattern that is desired. This mask will used to block light. Next, apply a layer of what is known as photoresist to the material that will be patterned. The photoresist is a light sensitive material. When exposed to light, it undergoes a chemical reaction that allows it to be easily removed by another chemical known as the developer. Thus it is known as photolithography because the photoresist's exposure to light is the key. So the photoresist covered material is exposed to light, but only in the areas not covered by the mask. After the developer is used, then those areas will have bare substrate.

Then those areas can be etched down further using other processes. Also note that there it is possible to use what is known as a negative photoresist instead. In that case, areas not exposed to light will be removed by the developer. Lastly, any excess photoresist is removed, and so just a patterned substrate remains. For details on all these processes, see [48].

3.3 Interferometric Photolithography

One problem that arises in standard photolithography is the difficulty in creating a physical mask. For structures with a very small periodicity, this can be prohibitive. To solve this, the technique of interferometric photolithography is used. It works by using a coherent light source, such as a laser, and interfering it with itself to create an interference pattern [49]. As an interference pattern, there will be peaks and nulls, and the nulls act as the mask. The photoresist areas with the nulls will not react, but the areas with the peaks will. Interfering coherent light at increasing larger angles allows for creation of very small periodicities in the photoresist. Then standard photolithography can be used to create a patterned substrate. In this work, silicon is used for the substrate upon which the desired thin-film material is deposited, due to its transmissive nature in the IR.

3.4 Glancing Angle Deposition

Glancing angle deposition (GLAD) is a technique for creating thin films that have a columnar nanostructure. The GLAD technique has been fairly recently developed, first being tested in the late 1990's by Robbie [50] [51]. In the last chapter, image of these nanocolumnar structures were shown, in Figs. 1, 5, and 6. The procedure for GLAD is fairly simple. The actual deposition is done by e-beam evaporation, a well known technique [52]. The deposition is performed on a substrate that is attached to

27

a tilted surface, which causes nanorods to "grow" at a set angle. Figure 9, modified from [27], shows this in a diagram.
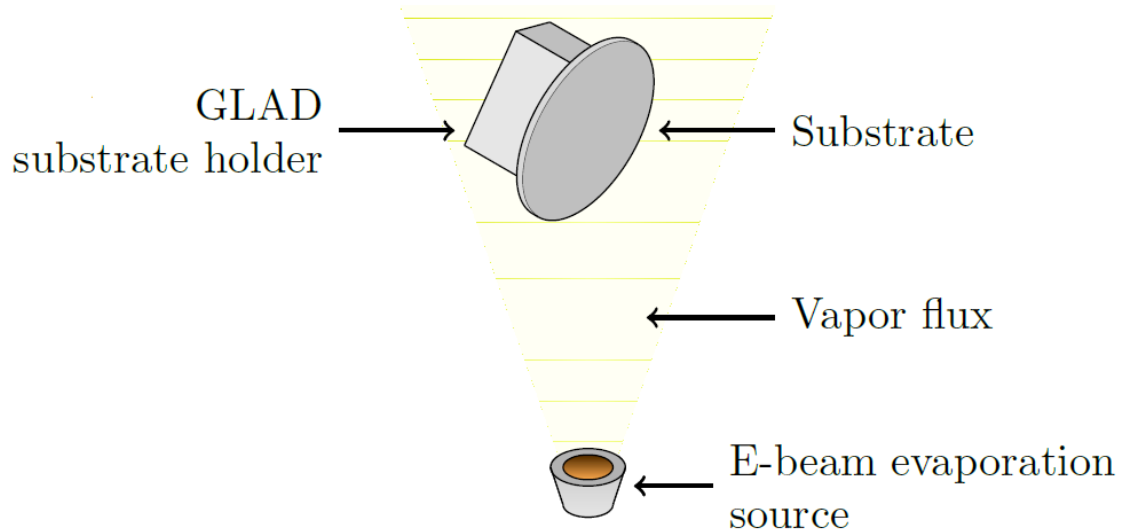
Figure 9. Diagram of Glancing Angle Deposition Process. The substrate is held at angle with respect to the e-beam evaporation source, which leads to the creation of an anisotropic metamaterial.

In a more advanced and recent technique from [53], it is possible to rotate the substrate during the deposition, which can produce more complex structures than rods, such as helices. This rotation will have the effect of making the nanorods grow at continuously varying angle.

Glancing angle deposition is a powerful technique for creating an anisotropic metamaterial with a known directionality. Now, if a patterned substrate obtained from the photolithography process is used as the substrate for the GLAD process, then the nanorods or nanohelicies will only grow on the higher areas on the substrate and not the etched down areas. This is due to the deposition at an angle, which leads to shadowing of the lower areas by the higher areas. Thus combining these two techniques results in an anisotropic photonic crystal metamaterial. Many different base materials

www.manaraa.com

can be used for the GLAD technique, like the ones covered in section 2.5. In this work vanadium oxide (V_yO_x), chromium (Cr), and germanium-antimony-tellurium (GST) were used. Vanadium oxide is referred to as V_yO_x, since it is known that vanadium is oxidized, but the exact oxidation state is not known. Future work will include more materials that have unique properties, which could open up even more possible applications. Another aspect to future work would be to quantitatively characterize the uncertainty in the deposition method. It is qualitatively clear from SEM images like Figure 1 in Section 2.1 that the size, shape, and angle of the nanostructures are not perfectly identical, leading to a non-uniform nature of the metamaterial, but the increase in uncertainty from this remains to be characterized.

3.5 Variable Angle Spectral Ellipsometry

To analyze this photonic crystal metamaterial experimentally, the technique of ellipsometry is used. Ellipsometry is a measurement technique that uses polarized light to characterize samples, such as thin films, bulk materials, and layered structures. It measures the relative phase change in polarization states of light reflected off (or transmitted through) the sample's surface. These measurements describe how samples modify the polarization state at each angle of incidence [32].

To understand what happens to the polarization state, it is important to know basic properties of reflection. It is known that the total reflection coefficients are the ratio of the amplitude of the reflected wave to the amplitude of the incident wave at different polarizations. For thin films, they are defined as

$$\mathbf{R}^p = \frac{r_{12}^p + r_{23}^p e^{-i2\beta}}{1 + r_{12}^p r_{23}^p e^{-i2\beta}} \tag{31}$$

$$\mathbf{R}^s = \frac{r_{12}^s + r_{23}^s e^{-i2\beta}}{1 + r_{12}^s r_{23}^s e^{-i2\beta}} \tag{32}$$

29

where the r with a subscript is the Fresnel reflection coefficient between the specified mediums, and β is the film phase thickness. The superscript p refers to the polarized wave in the plane (parallel polarization) and the superscript s refers to the polarized wave perpendicular to the plane of incidence (senkrecht polarization). Back in chapter 2, the notation TE and TM were used, and the correspondence of TE to p-polarization and TM to s-polarization can be made. The amplitude of both parallel and perpendicular components may be altered due to reflection of the sample. Eq. (31) and (32) represent the ratios of the reflected wave amplitude to the incident wave amplitude for both parallel and perpendicular components. Similar equations can be written for any arbitrary number of layers.

These reflection coefficients are related to the amplitude ratio, Ψ which is a value of interest from the experiment. First, define the complex quantity ρ to be the complex ratio of total reflection coefficients, R^p and R^s, such that $\rho = \frac{R^p}{R^s}$. Then $\rho = \tan(\Psi)$, and is clearly a measure of how much light is p-polarized versus s-polarized. Another value of interest is the total phase difference, Δ. The phase difference between both the parallel and perpendicular components of the incoming wave is referred to as δ_1 while the phase difference in the reflected wave is referred to as δ_2. To account for both of those, Δ is used and defined as $\Delta = \delta_1 - \delta_2$. Delta can change in phase difference upon reflection off the sample [32]. The process of ellipsometric measurement from light source to detector is shown in Figure 10 from [54].

In the case of the J. A. Wollam IR-VASE, the light source is a broadband infrared source. Typically, it is assumed that broadband light sources emit unpolarized light. The fixed polarizer converts the unpolarized light to a linear polarization and then the rotating compensator converts the linear polarization to an elliptical polarization which reflects off the sample. For the IR-VASE, these are wire-grid polarizers. Each polarizer has its own extinction function that is not in general flat spectrally. This is
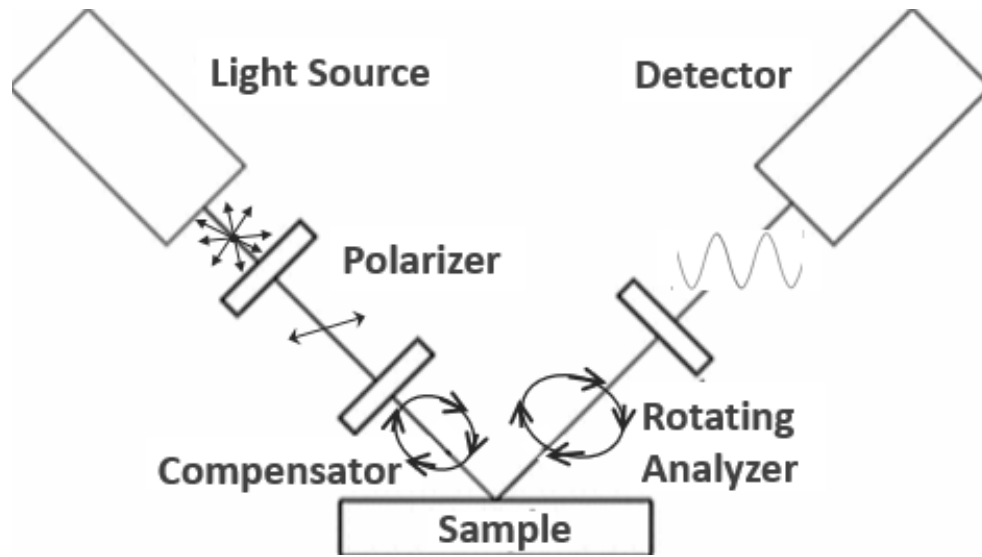
30

Figure 10. Diagram of the Ellipsometry Process. The polarizer and compensator produce circularly polarized light incident on the sample, and then the detector determines the precise polarization state of the reflection off the sample.

accounted for by the software when taking experimental data by measured responses with and without the polarizers in place. This calibration does not need to be performed every time the IR-VASE is used, since the polarizers are located inside the apparatus and thus do not change or degrade quickly.

Returning to Figure 10, the reflection off the sample can generate a phase shift and/or attenuate one or both of the passing wave components. The reflection off the sample will not generally produce a light beam linearly or circularly polarized, rather something elliptically polarized. These various shifts of the phases are influenced by the optical properties of the samples, such as the thickness of layers, material composition, temperature, and orientation. The reflected signal of the different polarization states will be determined by the detector after passing through the analyzer.

The spectral nature of the signal at the detector is analyzed using a Fourier transform infrared (FTIR) spectrometer, which works simultaneously over the range of interest. The wavenumber resolution of FTIR spectrometer can be selected, and

31

this work used 8 cm^{-1} as the spectral resolution.

In general, the detected signal is a voltage sinusoid with a DC offset in the form:

$$V(t) = DC + \alpha \cdot \cos(2\omega t) + \beta \cdot \sin(2\omega t) \tag{33}$$

The ellipsometer measures the voltage, and does the fast Fourier transform (FFT) to find the two quantities α and β which are the Fourier coefficients of the signal. They can be written in terms of Ψ and Δ values, and the value P, the input polarizer angle with respect to the plane of incidence [54]

$$\alpha = \frac{\tan^2(\Psi) - \tan^2(P)}{\tan^2(\Psi) + \tan^2(P)} \tag{34}$$

$$\beta = \frac{\tan^2(\Psi)\cos(\Delta)\tan(P)}{\tan^2(\Psi) + \tan^2(P)}. \tag{35}$$

Equations (34) and (35) can be inverted to obtain the ellipsometric parameters, Ψ and Δ, which are the terms used to characterize the sample [54]. This α and β measurement is repeated many times for the same P, usually between 10 and 100, to also calculate a measure of noise in the system. This noise in α and β can be converted to uncertainty in Ψ and Δ, thus there can be certainty that Ψ and Δ actually represent signal rather than noise. These Ψ and Δ measurements are essential, because the quantities combined with an assumed model are used to calculate the material properties, such as the optical constants and thickness. Note the calculated properties are as reliable as the model, meaning Ψ and Δ can be correct, but an incorrect model can make the calculated properties meaningless.

Once experimental data in the form of Ψ and Δ over the specified spectral range is obtained, then a model of the material is created in the software WVASE32 [54]. Each layer of a layered material is modeled separately. The software contains a database of

materials with bulk optical constants that can be used for each layer. When creating a layer, a material and a layer thickness is chosen. Once a basic model is created, the next step is to fit the model to match the experimental data. This is accomplished by calculating the mean squared error (MSE) between the model's predictions and the experimental data, and then adjusting fit parameters to minimize the MSE. The formula for MSE is

$$MSE = \sqrt{\frac{1}{2N - M} \sum_{j=1}^{N} \left[\left(\frac{\psi_j^{mod} - \psi_j^{exp}}{\sigma_{\psi,j}^{exp}} \right)^2 + \left(\frac{\Delta_j^{mod} - \Delta_j^{exp}}{\sigma_{\Delta,j}^{exp}} \right)^2 \right]}, \qquad (36)$$

where N is number of experimental data points, M is the number of fit parameters, and the rest of the equation calculates the differences between the model and experiment at each point and then divides by the standard deviation of the experimental measurements. Any of the optical constants or thicknesses of the layers can be selected as fit parameters, but the number of fit parameters should generally not exceed the number of layers. The minimization of the MSE through adjusting the fit parameters is an iterative process that can be repeated as many times as necessary to achieve a low MSE, though typically less than 100 iterations are needed if good starting points are chosen. Unfortunately, while there are good database entries for common materials such as silicon that give good starting points, the data on rarer materials is much less accurate. Even with that limitation, accurate model fits with an MSE less than 1 are achievable when the material is simple, such as a one layer material. All the above applies for isotropic materials or simple cases.

Now, when measuring an anisotropic material, there are certain changes. Anisotropic materials were usually not measured using ellipsometric techniques until the development of generalized ellipsometry by Schubert [55] [56]. The basic principles are exactly the same as above, but much more data is needed to accurately characterize

33

the sample. One of the complications is that the laboratory frame of reference is not aligned with the anisotropy of the sample. Recall section 2.2 where it is was stated that these materials are in general biaxial, having only three permittivity variables. However, unless the laboratory axes and optical axes of the sample are aligned, the dielectric tensor that the detector measures non-zero off-diagonal elements. Therefore, it is necessary to use settings that will give data about these off-diagonal elements in the laboratory frame. To do this, the Mueller matrix setting is used. The Mueller matrix is a way to fully characterize of polarization properties of a material. It is a 4x4 matrix, that can be multiplied by light represented as Stokes vectors, which contain the intensity, degree, and type of incident polarization, to determine what the resulting Stokes vector would be. For example, Mueller matrix calculus is often used for analyzing optical elements [57].

The setting takes enough data to calculate 12 of the 16 elements of the Mueller matrix, giving large amounts of data about the polarization response of the material. The four elements that are not calculated relate to circular polarization incident on the material. The reason these four elements cannot be calculated is that the compensator in the VASE setup does not rotate; in a dual rotating setup, where the compensator and the analyzer rotate, all 16 elements could be calculated. Still, fitting for all nine elements of the dielectric tensor simultaneously would be computationally expensive, so another method can be used to diagonalize the dielectric tensor. In effect, the data is translated from the laboratory frame, where there would be nine variables, to the sample frame, where there are only three. The angles which represent this transformation are known as the Euler angles. Figure 11 from [54] shows how the Euler angles are geometrically determined.
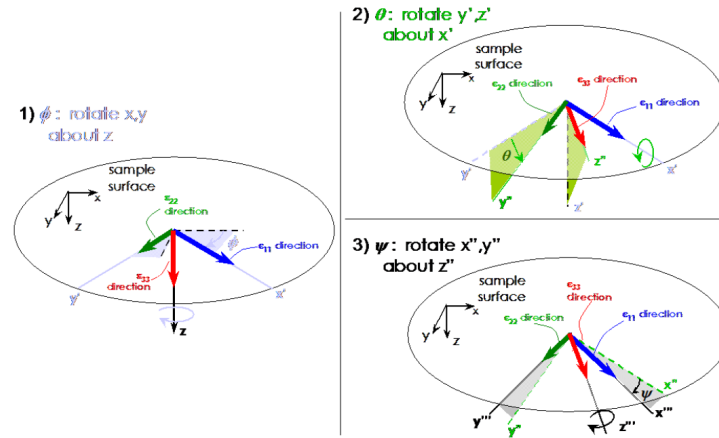
Figure 11. Diagram on Determining the Euler angles. To determine the Euler angles in a unique way, it is necessary to follow the diagram in order, from step 1 to step 2 to step 3.

Using the process shown in Figure 11, these Euler angles can be determined from the known geometry of the sample, and thus used to reduce the computational load. The Euler angles define a transformation matrix, which is multiplied by the laboratory dielectric tensor, which has non-zero off-diagonal elements, to transform it to the sample dielectric tensor, which has components only along the diagonal. The simplest way to find the value of the permittivity in each direction is to directly use it as a fit parameter in each direction, while assuming known Euler angles and layer thicknesses. Also note that the Euler angles themselves can be selected as fit parameters, which allows for a check that appropriate Euler angles were geometrically determined. The layer thicknesses can be determined from scanning electron microscopy (SEM).

It is also beneficial to couple the results of multiple measurements together to increase the accuracy of the final permittivities. In this work, measurements with a sample rotation, which corresponds to an Euler angle ϕ, of 0°, 45°, 90°, and 115° were coupled together to produce the final result. Note that Euler angles are unique for each measurement, so the coupling equations must be modified to take that into

35

account. Also note that the real and imaginary parts of the permittivity in each direction are fit separately, so there is a total of six unknown parameters for which to fit. Another way to find the permittivity which can be more accurate is to use a known oscillator model for the permittivity and then fit for the parameters of the model rather than the permittivity itself. Oscillator models such as the Lorentz oscillator [58] or Gaussian oscillator [59] could be used in the software WVASE32. As an example, the equation for Lorentz oscillators is

$$\epsilon(E) = \sum_{n=1}^{N} \frac{A_n Br_n E_n}{E_n^2 - E^2 - iBr_n E}, \tag{37}$$

where N is the number of oscillators, A_n is the amplitude of the nth oscillator, Br_n is the broadening of the nth oscillator, and E_n is the peak location of the nth oscillator. E is used since the WVASE32 software defaults to having the dielectric function be a function of photon energy, specifically eV. A similar equation can easily applied to frequency, wavelength, or wave number. So there are three parameters available to change the shape of the dielectric function when using a Lorentz oscillator. However, a single Lorentz oscillator is not nearly enough to model a complicated dielectric function, thus achieving an oscillator model that is close enough to the correct permittivity so the fitting process succeeds is very difficult, requiring complicated combinations of oscillators and highly precise starting parameter values. Therefore in this work, the permittivity is fit directly, rather than through an oscillator model. Even with this, a low MSE can be achieved.

The last problem is that of local minima in the fitting process. It often appears that different local minima can be found with a low MSE, but not the actual lowest possible. These different cases often have wildly different resultant permittivities. Therefore, physical intuition must be used to throw out cases that result in extreme permittivity values. Generally, there is only one case in which all the permittivity

36

values are physically possible, therefore the correct case is simple to determine. Thus the optical constants for anisotropic materials are calculated by determining the ψ and Δ for as many arbitrary polarizations and directions as possible, then applying the Euler angle transformation to reduce the number of variables, and lastly directly fitting for the optical constants by minimizing the MSE.

3.6   COMSOL Multiphysics

The permittivity of the different regions of the photonic crystal metamaterial is now well characterized, but the most critical property, that of the photonic bandgap, is not known. So to calculate the bandgaps, COMSOL Multiphysics®is used. COM-SOL Multiphysics is an interactive environment for modeling and simulating scientific and engineering problems. The program includes multiple modules that increase the functionality. One such module is the wave optics module, which is used in this work. The goal of the COMSOL simulation is to calculate the size of the photonic bandgap using the refractive index measurements from the ellipsometry process. The simulation is only of one 2D unit cell, but it uses periodic boundary conditions, also known as Floquet boundary conditions, to account for the effects of the other unit cells around it.
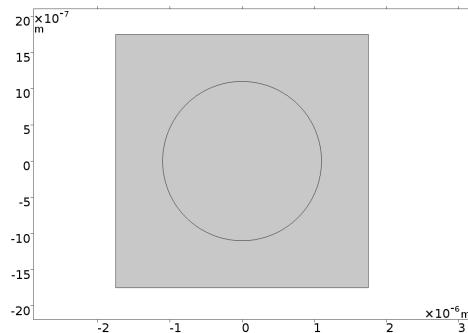

Figure 12. Plot of the 2D geometry of the unit cell used in COMSOL, with periodicity 3500 nm and air hole radius 1100 nm.

Figure 12 is an example where the lattice structure used is a square lattice. Region 1 is the circle in the center, for which the optical properties of air were used, and Region 2 is everything else in the unit cell, for which the optical properties of a metamaterial were used. The periodicity, which is the same as the unit cell side length, and the air hole radius can be changed, but the geometry in every case will look very similar to the case shown.

The permittivity of the non-air region must be known to perform the simulation, so the results from the ellipsometry were used as inputs to the simulation. The COMSOL simulation works along the same lines as the plane wave expansion technique discussed in section 2.5. However, there are some significant differences. The permittivity of the material being wavelength dependent leads to an issue with the designed eigenvalue solver. Therefore it becomes necessary to use the stationary solver instead, and insert equations that treat the eigenvalue as an unknown. This allows the obtaining of the correct eigenvalues even while sweeping every possible value of the wave vector. This does require the use of a non-linear solver, which does not always converge. Due to the lossy nature of materials involved, eigenvalues with a small imaginary component are derived. Using these complex values as inputs to the non-linear solver can sometimes lead to a lack of convergence. Still, in most cases, the simulations successfully converge.

So using this simulation, it is possible to fairly efficiently find the photonic bandgaps for a characterized anisotropic material and photonic crystal structure. The bandgap structure was determined for in-plane case, with the electric field parallel to plane of incidence (TE), and the out-of-plane case, with the electric field perpendicular to plane of incidence (TM). For a 2D system, this covers all necessary cases. So it is not necessary to account for oblique angles of incidence in this work.

3.7 Summary

In summary, the fabrication methods for creating photonic crystal metamaterial samples were covered, including interferometric photolithography and glancing angle deposition. Then the experimental method was established, and lastly the computational method was discussed. Now that the methodology is known, the results can be presented.

IV. Results and Discussion

4.1 Chapter Overview

In this chapter, the results of this work are covered and discussed. First, the results of ellipsometry and discussion of the accuracy and applicability of these results, and then the results of the COMSOL simulations and a discussion of the accuracy and applicability of these results are presented.

4.2 Ellipsometry Results and Discussion

First, the characteristics of selected metamaterial samples are shown in Figures 13-14 using scanning electron microscope (SEM) images. Figure 13 demonstrates that there is a structure that can be easily aligned with the traditional axis system, where z, which is the extraordinary transmission direction, points along the central axis of the nanohelicies. Figure 14 shows that the nanorod structure is not easily aligned with a laboratory coordinate system, so Euler angle transformations must be used. There is no SEM image of the Cr nanohelix sample; the image would likely be very similar to the V_yO_x SEM image.
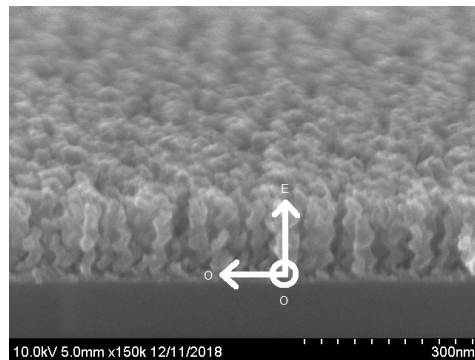

Figure 13. SEM image of V_yO_x nanohelix sample with labeled sample axes, taken by Dr. Sarangan at the University of Dayton. Used with permission.
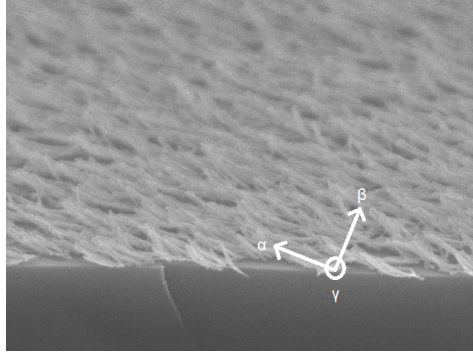
40

Figure 14. SEM image of GST nanorod sample with labeled sample axes, taken by Dr. Sarangan at the University of Dayton. Used with permission.

Figures 15-20 are the optical constants of the anisotropic metamaterials with no photonic crystal structure, fabricated with the technique from section 3.4, with results obtained using the ellipsometry process detailed in section 3.5. These will be used as inputs in the computational simulation. The shaded regions show the 90% confidence interval for the values, which corresponds to 1.645σ in terms of the normal distribution. Note that this uncertainty is completely different than the MSE described in section 3.5, specifically Eq. (36). The MSE is a value that describes how well the VASE model fits with the experimental data, with a smaller MSE indicating a better fit. The 90% confidence intervals come from the noise in the system at each spectral point, and do not characterize the quality of fit, but rather the regions of confidence in the optical constant values.

In Figure 15, there is clearly a large difference between the ordinary and extraordinary directions in the V_yO_x sample, as expected. This large difference in optical properties between different directions leads to a large birefringence in the sample, since the birefringence is defined as the maximum difference between the two optical properties in the different directions, $n_O - n_E$. This plot shows an approximate maximum birefringence of 3, which is higher than any natural crystals, as discussed in

41

section 2.6. This allows higher effectiveness in applications that require birefringence, and a larger complete photonic bandgap. Also note that the confidence intervals widen as the wavelength increases. This is because the resolution of the FTIR is in wavenumber (cm^{-1}), so as the wavelength increases, the density of the experimental data decreases. Overall, these results are somewhat different than expected, since in most other cases of GLAD fabricated metamaterials, such as the materials discussed in section 2.6, the real index is higher in the extraordinary direction than the ordinary direction, while the opposite is observed in Figure 15. However, this phenomenon was only observed in nanorod structured metamaterials, and nanohelix structured metamaterials have not been studied before. Thus it is possible that for nanohelix metamaterials, the ordinary direction has a larger index than the extraordinary direction. More research is needed to confirm the accuracy of this result, which is planned for the future.

In Figure 16, note that the k values, which correspond to attenuation in the sample, are non-zero, thus the material is lossy. This is expected, as it is composed mostly of a metal. The total mean-squared error (MSE), or in other words quality of fit parameter, for this material, when selecting for all four unknown indices as fit parameters, is 1.233. The Euler angles used were $0°$, $45°$, $90°$, and $115°$ for ϕ, $180°$ for θ, and $0°$ for ψ. When selecting these as fit parameters to verify, the Euler angles received were -0.279°, 45.176°, 90.419°, and 114.532° for ϕ, 180.495° for θ, and 0.488° for ψ, which are very close to geometrically derived Euler angles. Thus it can be seen that the Euler angle uncertainty is about 1 degrees, which is reasonable considering the fabrication tolerances.
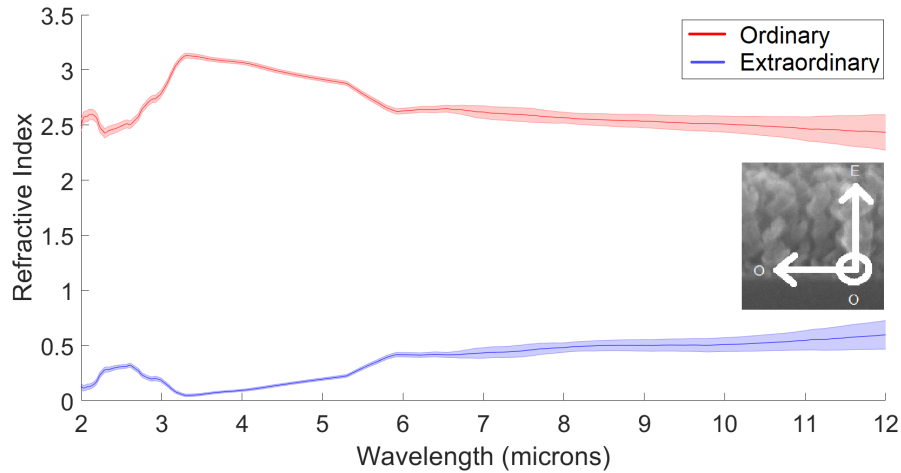
Figure 15. Real index of refraction (n) of V_yO_x metamaterial along the two axes, from 2 to 12 microns, with 90% confidence intervals.
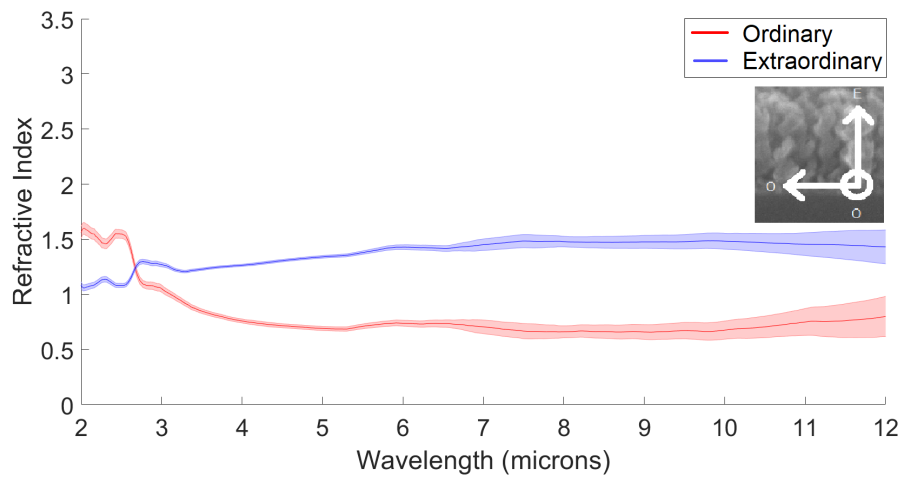

Figure 16. Imaginary index of refraction (k) of V_yO_x metamaterial along the two axes, from 2 to 12 microns, with 90% confidence intervals.

In Figure 17, the birefringence is much lower, except in the very low wavelength ranges. This could mean that Cr metamaterials are more suited to the visible regime rather than IR, which is the regime studied in previous work discussed in section 2.6. Thus it is not possible to directly compare to previous work. In Figure 18, as Cr

43

is a pure metal that is not oxidized, the k value rises drastically, which is expected. However, it is unexpected that this would only occur for the ordinary direction and not both directions. One possibility is that since Cr is a pure metal and not oxidized, the magnetic properties are significant, especially along the direction of nanohelicies, so the extraordinary direction could be inaccurate for that reason. More research is needed, and is planned for the future. The total mean-squared error (MSE) for this material, when fitting for all four unknown indices, is 1.555. The Euler angles used were 0°, 45°, 90°, and 115° for ϕ, 180° for θ, and 0° for ψ. When selecting these as fit parameters to verify, the Euler angles received were 0.589°, 45.772°, 89.288°, and 115.424° for ϕ, 179.483° for θ, and -0.530° for ψ, which are within about 1 degree of the geometrically dervied Euler angles.
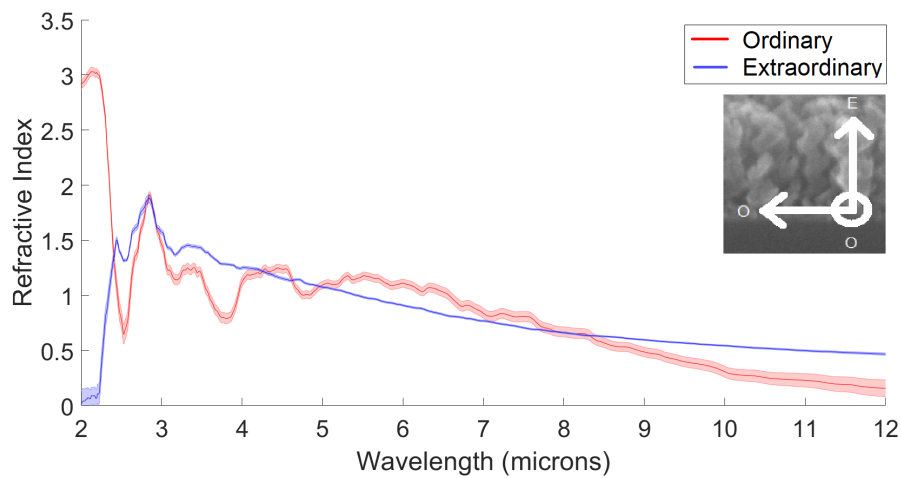

Figure 17. Real index of refraction (n) of Cr metamaterial along the two axes, from 2 to 12 microns, with 90% confidence intervals.
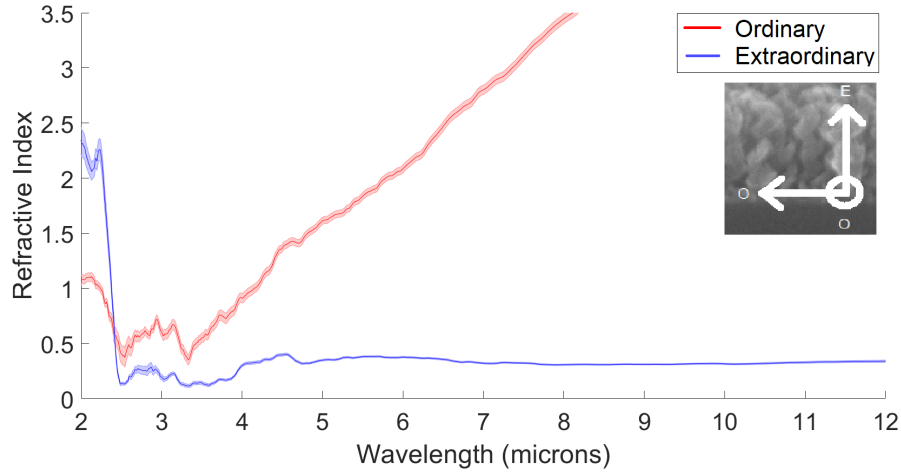
Figure 18. Imaginary index of refraction (k) of Cr metamaterial along the two axes, from 2 to 12 microns, with 90% confidence intervals.

In Figure 19, it is clear that the uncertainty is much higher in the α direction, which corresponds to the direction of the nanorods. This is an interesting result that has not been stated in any previous work, since the results in those cases were presented without error estimates, as seen in section 2.6. It makes some sense, as that direction is where the metamaterial effects should be most readily observed. Also note that the birefringence is around 1 for most of the spectral range, which is still higher than most natural materials. In Figure 20, at large wavelengths, the k values in each direction become small. This is a positive for applications, as devices formed of this material would be more efficient. The measured uncertainty below 3 microns was larger than the allowed tolerance from the software, so that data was not included in the fitting process. When comparing to the data from previous work shown in Figure 4 in section 2.6, the β and γ directions show very similar behavior to the measured amorphous state data. This lends confidence to the results. Also, the indicies are higher along the direction of the nanorods than the other directions, which is again the same as previous work discussed in section 2.6, and seen in Figures

45

6 and 8. The total mean-squared error (MSE) for this material, when fitting for all six unknown indices, is 0.985. The Euler angles used were 0°, 45°, 90°, and 115° for ϕ, 13° for θ, and 0° for ψ. When selecting these as fit parameters to verify, the Euler angles received were 0.523°, 44.219°, 90.075°, and 114.119° for ϕ, 13.183° for θ, and -5.5364° for ψ. The ψ value when fitting is somewhat different than the geometric value, which should be 0°. This is most likely due to fabrication defects. However, using the value of 0 or -5.5364 for ψ does not greatly change the derived optical constants, so geometric value of 0 was used in this work.
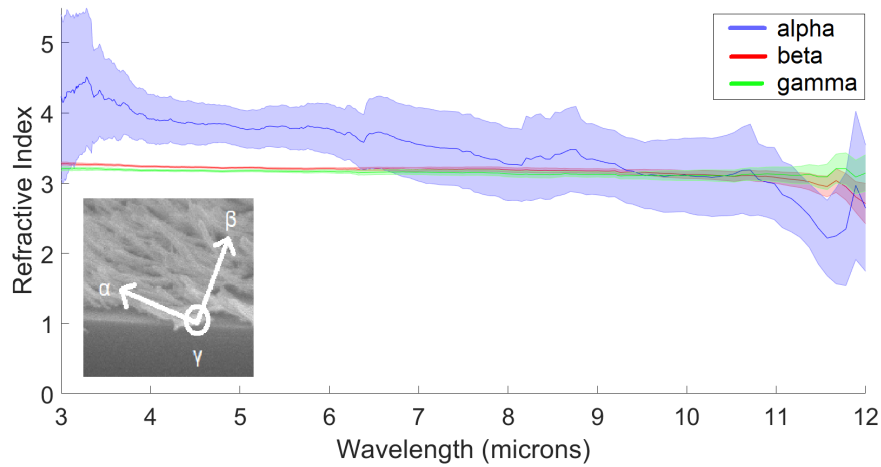

Figure 19. Real index of refraction (n) of GST metamaterial along the three axes, from 3 to 12 microns, with 90% confidence intervals.
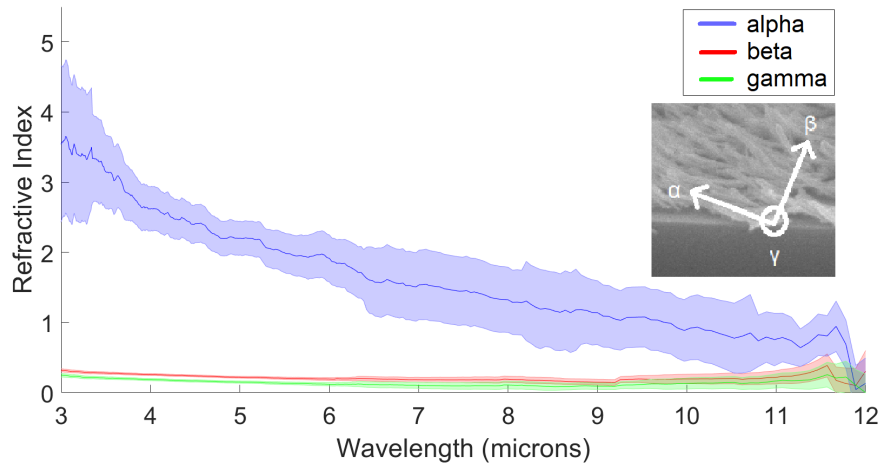
Figure 20. Imaginary index of refraction (k) of GST metamaterial along the three axes, from 3 to 12 microns, with 90% confidence intervals.

In total, accurate optical constants for novel metamaterials design were obtained, which by itself is a useful achievement, since measurements of these specific nanohelical and nanocolumnar metamaterials have not been published before. Also, this work is one of the first to present error bars along with the optical constants data, which raises confidence in the results.

4.3 COMSOL Results and Discussion

Figure 21 shows the results of the COMSOL simulation for a photonic crystal metamaterial. The 2D photonic crystal structure used is a square lattice, with circular air holes at the lattice points. The photonic crystal structure was chosen based on feasibility of fabrication of a physical photonic crystal metamaterial with that structure. The measured optical constants of the Cr metamaterial are used as inputs for the non-air hole region. The lowest ten bands in the TE and TM polarizations were calculated. There are not always ten different band lines, however, because the eigenvalues are often degenerate. Note that all the following figures are shown with

two y-axes, a frequency y-axis, and a dimensionless y-axis defined as $\frac{af}{c}$, where a is periodic spacing, f is the frequency, and c is the speed of light. This dimensionless frequency axis is the standard for photonic band diagrams. Also define b to be the radius of the air holes. In this case, $a = 3500$ nm and $b = 700$ nm. This periodicity was chosen to make sure that the photonic bandgap would be in the region where the optical constants are known. Since the optical constants are known for above 2000 nm, the periodicity should be on that order of magnitude. From Figure 21, it can be seen that the lower frequency region, which is the higher wavelength region, looks very similar for the TE and TM polarizations. This makes sense, since the difference between optical constants in that region from Figure 17 is small. In the low wavelength region, the difference is large, and the band structure is different. This simulation shows a low frequency bandgap in the TE polarization, and a high frequency bandgap in the TM polarization, but no complete bandgap.
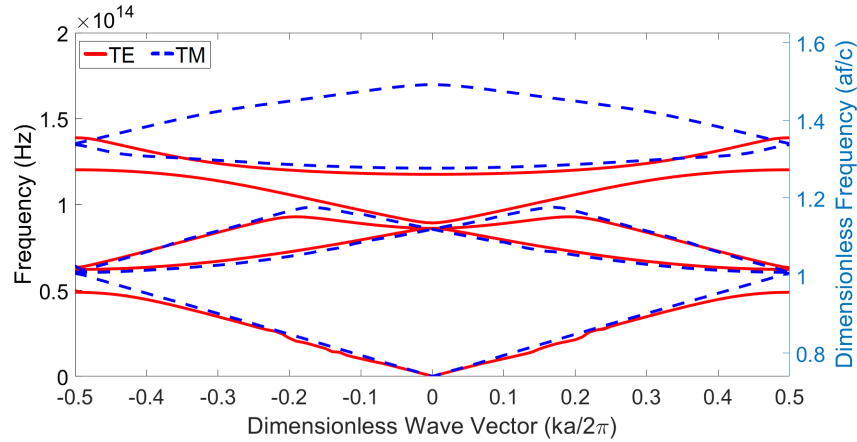

Figure 21. COMSOL simulation results of Cr photonic crystal metamaterial with $a = 3500$ nm and $b = 700$ nm.

Now, for the base metamaterial V_yO_x, tests were performed where the parameters a and b were varied for the same lattice structure as before. Table 1 shows a summary of the cases covered, and whether the non-linear solver converged in that case. In

48

Table 1, the 2D fill fraction is calculated from the formula

$$FF = \frac{a^2 - \pi b^2}{a^2} \tag{38}$$

From Table 1, it can be seen that the TE polarization cases converged more often than the TM polarization cases. Also, only the small filling fractions in the 2500 nm spacing case failed to converge. This suggests that this method will be more successful with larger filling fractions.

Table 1. Details of V_yO_x Cases Covered and their Convergence

Case #	Periodicity (nm)	Hole Radius (nm)	2D Fill Fraction	TE?	TM?
1	2500	300	0.95	Yes	Yes
2	2500	500	0.87	Yes	Yes
3	2500	700	0.75	Yes	No
4	2500	900	0.59	Yes	No
5	2500	1100	0.39	No	No
6	3500	300	0.98	Yes	Yes
7	3500	500	0.94	Yes	Yes
8	3500	700	0.87	Yes	Yes
9	3500	900	0.79	Yes	Yes
10	3500	1100	0.69	Yes	Yes

Figures 22-30 show the results of the COMSOL simulation in each case. From Figures 22-30, it is clear that the periodicity and air hole radius have a large impact on the photonic band structure. There are complete bandgaps in a few cases, namely Case 1 (Figure 22) and Case 10 (Figure 30), but in general, the bandgaps in the TE and TM modes do not line up. This is expected when the a and b parameters

49

are not optimized for the presence of a complete photonic bandgap. Recall the gap-midgap ratio, R_g, defined in section 2.4. The complete bandgap in Case 1 (Figure 22) has a gap-midgap ratio of 0.125, which is fairly large, as in previous work [60], a gap-midgap ratio of 0.2 was the highest achieved for a square lattice even after a significant amount of optimization. There are actually two complete bandgaps in Case 10 (Figure 30), with the lower one having a gap-midgap ratio of 0.077, and the higher one having a gap-midgap ratio of 0.053. These are slightly smaller than Case 1, but having two complete bandgaps could be a useful property. It is possible to observe that the TE polarization has larger bandgaps in almost every case, which most likely comes from the index of refraction being higher in the extraordinary direction, which gives a stronger contrast to the index of refraction of air. Thus it may be useful in the future to calculate more bands with the TM polarization, so higher frequencies can be explored.
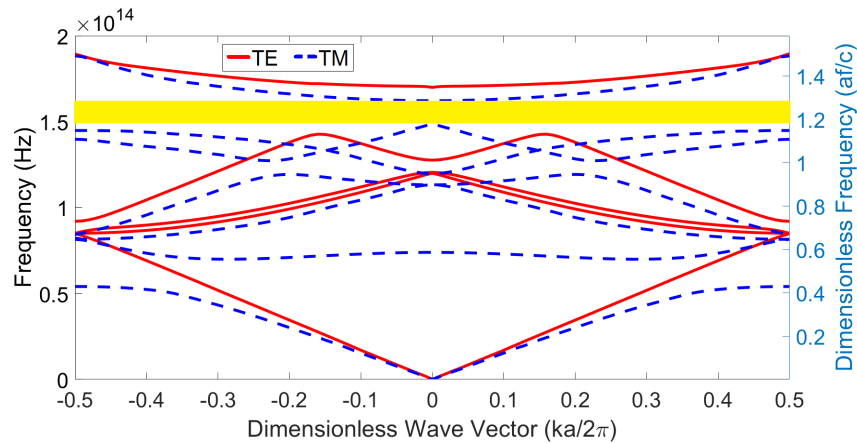

Figure 22. COMSOL simulation results of V_yO_x photonic crystal metamaterial with $a = 2500$ nm and $b = 300$ nm.
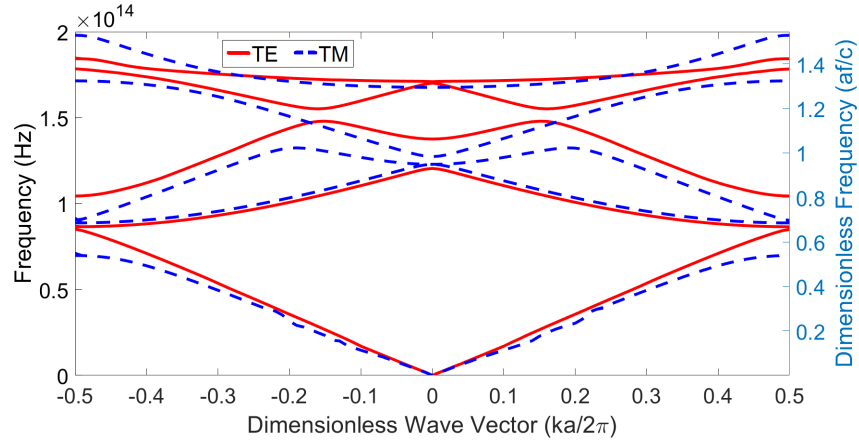
50

Figure 23. COMSOL simulation results of V_yO_x photonic crystal metamaterial with $a = 2500$ nm and $b = 500$ nm.

Figure 24. COMSOL simulation results of V_yO_x photonic crystal metamaterial with $a = 2500$ nm and $b = 700$ nm. The TM polarization did not converge.
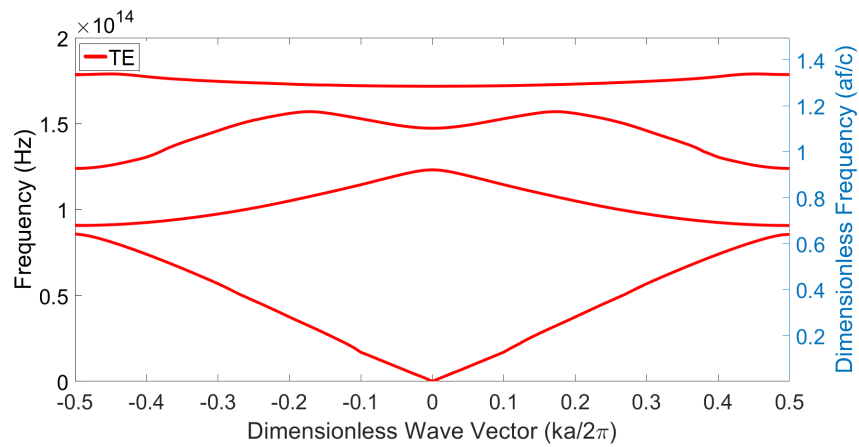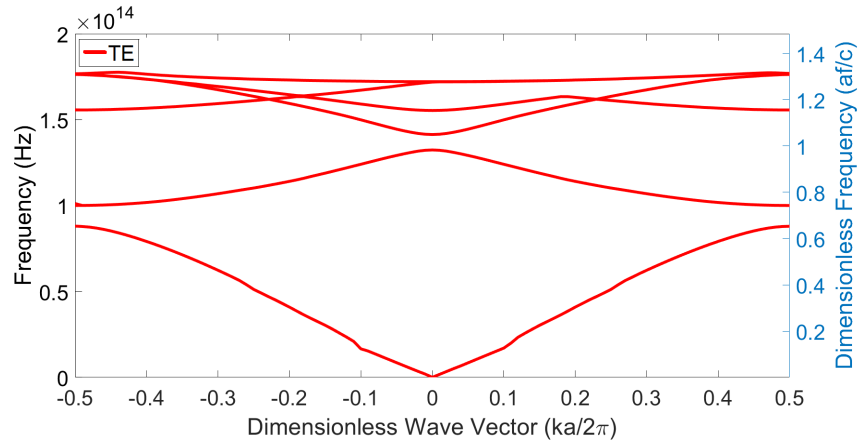
51

Figure 25. COMSOL simulation results of V_yO_x photonic crystal metamaterial with $a = 2500$ nm and $b = 900$ nm. The TM polarization did not converge.
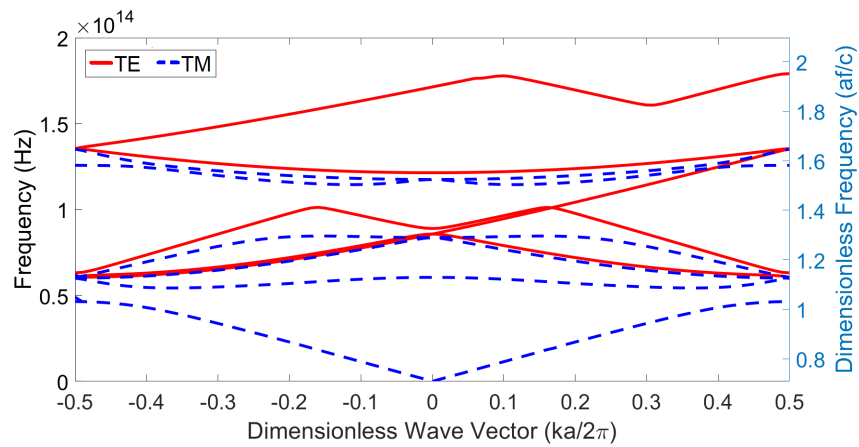

Figure 26. COMSOL simulation results of V_yO_x photonic crystal metamaterial with $a = 3500$ nm and $b = 300$ nm.

52
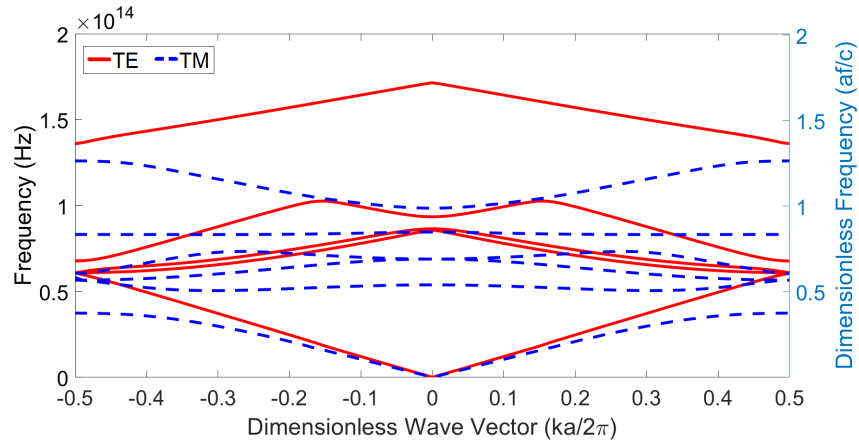
Figure 27. COMSOL simulation results of V_yO_x photonic crystal metamaterial with $a = 3500$ nm and $b = 500$ nm.

Figure 28. COMSOL simulation results of V_yO_x photonic crystal metamaterial with $a = 3500$ nm and $b = 700$ nm.
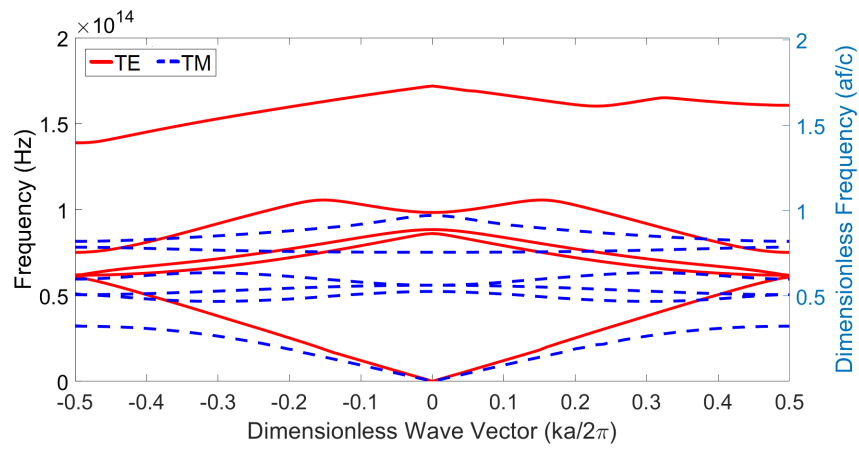
53
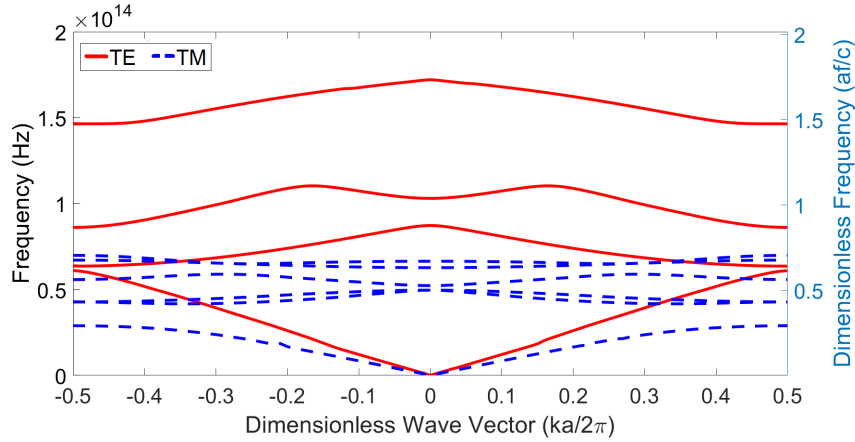
Figure 29. COMSOL simulation results of V_yO_x photonic crystal metamaterial with $a = 3500$ nm and $b = 900$ nm.
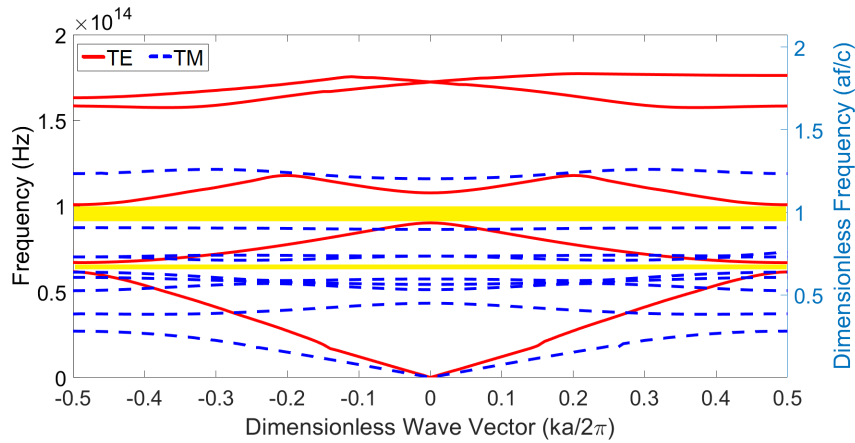
Figure 30. COMSOL simulation results of V_yO_x photonic crystal metamaterial with $a = 3500$ nm and $b = 1100$ nm.

From all these band diagrams, it is clear that many various band structures are possible, just by changing a few parameters of the geometry. It is possible to vary the parameters much more than is done in this work, and future work should involve optimization over large parameter spaces. For example, a completely different unit cell, like a triangular or hexagonal unit cell could be used. This has been done before for the case of photonic crystals composed of natural materials, but not for

54

photonic crystals composed of metamaterials. These metamaterials have much higher birefringence than natural materials, so theoretically, much larger complete bandgaps could be achieved. This would allow for much wider band operation of photonic devices, which would increase the applicability of such devices immensely. Also, the use of metamaterials allows for much more customizability, since almost any material can be used as the base material for the GLAD process. So a material that has desirable properties in its bulk form could be converted to an anisotropic metamaterial and used in photonic devices.

Now that the possibilities of photonic crystal metamaterials are known, it is important to establish that such devices are actually physically realizable. To do this, the techniques described in Sections 3.2 and 3.3 were used to create photonic crystal metamaterials, which successfully verifies that these new developments can be practically used. These devices are to be empirically characterized in the near future.

4.4   Summary

In summary, the optical constant results of the ellipsometry process for the non-photonic crystal metamaterial samples were covered, showing large birefringence values in most cases. Uncertainty bounds for these retrieved values were included for the 1st time. After that, the computational results were covered and compared to experimental results for verification purposes. Since the results have been discussed, next the conclusions are presented.

55

V. Conclusion

5.1 Conclusions of Research

In conclusion, the development of photonic crystal metamaterials has clearly been advanced. First, accurate optical constants of novel metamaterials fabricated by glancing angle deposition have been found using ellipsometry, which demonstrate the high birefringence necessary for complete photonic bandgaps. Next, simulations of the metamaterials with a photonic crystal were performed using COMSOL Multiphysics, which showed design of complete photonic bandgaps is possible. Next, these results were shown to be physically realizable by fabricating photonic crystal metamaterials by combining interferometric photolithography and glancing angle deposition. Thus the first demonstration of complete photonic bandgaps using a 2D anisotropic photonic crystal metamaterial was achieved. Now that this has been achieved, applications that make use of photonic bandgaps, such as optical communications, optical computing, and directed energy can start to make use of this new capability in new devices and products.

5.2 Recommendations for Future Research

In the near future, it is important to verify and expand the results of this work by retaking this data and taking data on similar metamaterials. Much work remains to be done on photonic crystal metamaterials, with this work only representing one of the first steps. There are three main avenues of research that should be pursued to develop this technology further. First, the utilization of unique base materials. Second, design optimization through computational simulation. Third, empirical design principles that can guide applications.

Regarding the first path, unique base materials such as V_yO_x and GST have

56

already been used in this work, but they have not yet been utilized to their full extent. Materials such as V_yO_x and GST are known as phase change materials because their properties can drastically change with temperature while still remaining solid. This type of material could have many applications in situations where temperature gradients are present.

The next avenue of computational design optimization could yield incredible results for specific applications. The process has been done for photonic crystal with natural materials, but it has not been for photonic crystal metamaterials. A similar process to previous work could be followed, where many different filling ratios, lattice structures, and periodicities could be tested under some sort of optimization algorithm, such as a particle swarm or a genetic algorithm. For example, a hexagonal lattice structure would most likely be more efficient.

The last path of creating empirical design principles that can be used by those not familiar with the full theory of photonic crystals and metamaterials is certainly the most difficult. There are in actuality two parts to this path, the first is relating what is directly known after fabrication to the properties of a non-photonic crystal metamaterial. This is quite difficult because the metamaterial properties are always different than the bulk material properties. One possibly fruitful avenue is to modify mixing formulas to account for metamaterial nature of the GLAD produced sample. The next step is take those metamaterial properties and determine what the properties of a photonic crystal using that metamaterial as a base would have. For this step, it should be possible to just use the computational design optimization that was developed beforehand.

Final recommendations include more research on 3D photonic crystals and metamaterials, which could theoretically could be combined in a similar way to this work. More research on metamaterials in general is required to achieve fully controllable

optical properties.

Bibliography

1. T. A. Birks, J. C. Knight, and P. S. J. Russell, "Endlessly single-mode photonic crystal fiber," *Optics letters*, vol. 22, no. 13, pp. 961–963, 1997.

2. J. M. Dudley, G. Genty, and S. Coen, "Supercontinuum generation in photonic crystal fiber," *Reviews of modern physics*, vol. 78, no. 4, p. 1135, 2006.

3. J. Knight, J. Arriaga, T. Birks, A. Ortigosa-Blanch, W. Wadsworth, and P. S. J. Russell, "Anomalous dispersion in photonic crystal fiber," *IEEE photonics technology letters*, vol. 12, no. 7, pp. 807–809, 2000.

4. P. Russell, "Photonic crystal fibers," *science*, vol. 299, no. 5605, pp. 358–362, 2003.

5. A. Silva, F. Monticone, G. Castaldi, V. Galdi, A. Alù, and N. Engheta, "Performing mathematical operations with metamaterials," *Science*, vol. 343, no. 6167, pp. 160–163, 2014.

6. K. Iwaszczuk, A. C. Strikwerda, K. Fan, X. Zhang, R. D. Averitt, and P. U. Jepsen, "Flexible metamaterial absorbers for stealth applications at terahertz frequencies," *Optics express*, vol. 20, no. 1, pp. 635–643, 2012.

7. J. Kim, K. Han, and J. W. Hahn, "Selective dual-band metamaterial perfect absorber for infrared stealth technology," *Scientific reports*, vol. 7, no. 1, p. 6740, 2017.

8. Y. Fink, J. N. Winn, S. Fan, C. Chen, J. Michel, J. D. Joannopoulos, and E. L. Thomas, "A dielectric omnidirectional reflector," *Science*, vol. 282, no. 5394, pp. 1679–1682, 1998.

9. J. N. Winn, Y. Fink, S. Fan, and J. Joannopoulos, "Omnidirectional reflection from a one-dimensional photonic crystal," *Optics letters*, vol. 23, no. 20, pp. 1573–1575, 1998.

10. E. Cojocaru, "Omnidirectional reflection from finite periodic and fibonacci quasi-periodic multilayers of alternating isotropic and birefringent thin films," *Applied optics*, vol. 41, no. 4, pp. 747–755, 2002.

11. S. Shi, C. Chen, and D. W. Prather, "Plane-wave expansion method for calculating band structure of photonic crystal slabs with perfectly matched layers," *JOSA A*, vol. 21, no. 9, pp. 1769–1775, 2004.

12. Z.-Y. Li and L.-L. Lin, "Photonic band structures solved by a plane-wave-based transfer-matrix method," *Physical Review E*, vol. 67, no. 4, p. 046607, 2003.

13. J. Yuan and Y. Y. Lu, "Photonic bandgap calculations with dirichlet-to-neumann maps," *JOSA A*, vol. 23, no. 12, pp. 3217–3222, 2006.

14. Z.-Y. Li, B.-Y. Gu, and G.-Z. Yang, "Large absolute band gap in 2d anisotropic photonic crystals," *Physical Review Letters*, vol. 81, no. 12, p. 2574, 1998.

15. Z.-Y. Li, B.-Y. Gu, and G.-Z. Yang, "Improvement of absolute band gaps in 2d photonic crystals by anisotropy in dielectricity," *The European Physical Journal B-Condensed Matter and Complex Systems*, vol. 11, no. 1, pp. 65–73, 1999.

16. S.-W. Wang, W. Lu, X.-S. Chen, M. Zhou, and X.-C. Shen, "Photonic band gap in two-dimensional anisotropic photonic crystal with rectangular bars," *International Journal of Infrared and Millimeter Waves*, vol. 24, no. 6, pp. 963–971, 2003.

17. H. Xie and Y. Y. Lu, "Modeling two-dimensional anisotropic photonic crystals by dirichlet-to-neumann maps," *JOSA A*, vol. 26, no. 7, pp. 1606–1614, 2009.

18. H. A. G. Urrea, C. A. D. Echeverri, and M. E. M. Ramos, "Two dimensional photonic crystals based on uniaxial polar materials: Influence of the shape of the dielectric polaritonic core," in *Latin America Optics and Photonics Conference*, pp. LTu4A–48, Optical Society of America, 2016.

19. H. Gómez-Urrea, C. Duque, and M. Mora-Ramos, "The polaritonic spectrum of two-dimensional photonic crystals based on uniaxial polar materials," *Superlattices and Microstructures*, vol. 87, pp. 58–63, 2015.

20. G. Alagappan, X. Sun, P. Shum, M. Yu, and D. den Engelsen, "Symmetry properties of two-dimensional anisotropic photonic crystals," *JOSA A*, vol. 23, no. 8, pp. 2002–2013, 2006.

21. I. A. Khromova and L. A. Melnikov, "Dispersion and symmetry properties of anisotropic photonic crystals of arbitrary geometry and dimension," in *Photonic Crystal Materials and Devices VIII*, vol. 6989, p. 69891V, International Society for Optics and Photonics, 2008.

22. R. P. Zaccaria, P. Verma, S. Kawaguchi, S. Shoji, and S. Kawata, "Manipulating full photonic band gap in two dimensional birefringent photonic crystals," *Optics express*, vol. 16, no. 19, pp. 14812–14820, 2008.

23. H. F. Zhang, S. Liu, and X.-K. Kong, "Properties of anisotropic photonic band gaps in three-dimensional plasma photonic crystals containing the uniaxial material with different lattices," *Progress In Electromagnetics Research*, vol. 141, pp. 267–289, 2013.

24. K. Kaminska and K. Robbie, "Birefringent omnidirectional reflector," *Applied optics*, vol. 43, no. 7, pp. 1570–1576, 2004.

25. K. G. Balmain, A. Luttgen, and P. C. Kremer, "Power flow for resonance cone phenomena in planar anisotropic metamaterials," *IEEE Transactions on Antennas and Propagation*, vol. 51, no. 10, pp. 2612–2618, 2003.

26. H. Tao, A. Strikwerda, K. Fan, W. Padilla, X. Zhang, and R. Averitt, "Reconfigurable terahertz metamaterials," *Physical review letters*, vol. 103, no. 14, p. 147401, 2009.

27. M. Benson, P. Shah, M. Marciniak, A. Sarangan, and A. Urbas, "Optical characterization of silver nanorod thin films grown using oblique angle deposition," *Journal of Nanomaterials*, vol. 2014, p. 4, 2014.

28. D. Schmidt, B. Booso, T. Hofmann, E. Schubert, A. Sarangan, and M. Schubert, "Generalized ellipsometry for monoclinic absorbing materials: determination of optical constants of cr columnar thin films," *Optics letters*, vol. 34, no. 7, pp. 992–994, 2009.

29. D. Schmidt, B. Booso, T. Hofmann, E. Schubert, A. Sarangan, and M. Schubert, "Monoclinic optical constants, birefringence, and dichroism of slanted titanium nanocolumns determined by generalized ellipsometry," *Applied Physics Letters*, vol. 94, no. 1, p. 011914, 2009.

30. W. Zhang and W. Zhao, "Birefringence in photonic crystal structures: Toward ultracompact wave plates," in *Advances in Photonic Crystals*, InTech, 2013.

31. S. R. Kennedy and M. J. Brett, "Porous broadband antireflection coating by glancing angle deposition," *Applied optics*, vol. 42, no. 22, pp. 4573–4579, 2003.

32. H. Tompkins and E. A. Irene, *Handbook of ellipsometry*. William Andrew, 2005.

33. V. Dmitriev, "Tables of the second rank constitutive tensors for linear homogeneous media described by the point magnetic groups of symmetry," *Progress In Electromagnetics Research*, vol. 28, pp. 43–95, 2000.

34. J. P. McKelvey, *Solid State Physics for Engineering and Materials Science*. Krieger Publishing Company, 1993.

35. P. Sivarajah, A. Maznev, B. Ofori-Okai, and K. Nelson, "What is the brillouin zone of an anisotropic photonic crystal?," *Physical Review B*, vol. 93, no. 5, p. 054204, 2016.

36. J. D. Joannopoulos, S. G. Johnson, J. N. Winn, and R. D. Meade, *Photonic Crystals: Molding the Flow of Light*. Princeton University Press, 2011.

37. B. Jiang, A. Liu, W. Chen, M. Xing, W. Zhou, and W. Zheng, "The optimization of large gap–midgap ratio photonic crystal with improved bisection-particle swarm optimization," *Optics Communications*, vol. 284, no. 1, pp. 226–230, 2011.

38. A. J. Danner, "An introduction to the plane wave expansion method for calculating photonic crystal band diagrams,"

39. A. Lavrinenko, P. I. Borel, L. H. Frandsen, M. Thorhauge, A. Harpøth, M. Kristensen, T. Niemi, and H. Chong, "Comprehensive fdtd modelling of photonic crystal waveguide components," *Optics Express*, vol. 12, no. 2, pp. 234–248, 2004.

40. F. Bréchet, J. Marcou, D. Pagnoux, and P. Roy, "Complete analysis of the characteristics of propagation into photonic crystal fibers, by the finite element method," *Optical Fiber Technology*, vol. 6, no. 2, pp. 181–191, 2000.

41. E. E. Chain, "Optical properties of vanadium dioxide and vanadium pentoxide thin films," *Applied optics*, vol. 30, no. 19, pp. 2782–2787, 1991.

42. S.-Y. Kim, S. J. Kim, H. Seo, and M. R. Kim, "Variation of the complex refractive indices with sb-addition in ge-sb-te alloy and their wavelength dependence," in *Optical Data Storage'98*, vol. 3401, pp. 112–116, International Society for Optics and Photonics, 1998.

43. J. N. Hilfiker, N. Singh, T. Tiwald, D. Convey, S. M. Smith, J. H. Baker, and H. G. Tompkins, "Survey of methods to characterize thin absorbing films with spectroscopic ellipsometry," *Thin Solid Films*, vol. 516, no. 22, pp. 7979–7989, 2008.

44. P. B. Johnson and R. W. Christy, "Optical constants of transition metals: Ti, v, cr, mn, fe, co, ni, and pd," *Phys. Rev. B*, vol. 9, pp. 5056–5070, Jun 1974.

45. H. U. Yang, J. D'Archangel, M. L. Sundheimer, E. Tucker, G. D. Boreman, and M. B. Raschke, "Optical dielectric function of silver," *Phys. Rev. B*, vol. 91, p. 235137, Jun 2015.

46. C. F. Buhrer, L. Bloom, and D. Baird, "Electro-optic light modulation with cubic crystals," *Applied Optics*, vol. 2, no. 8, pp. 839–846, 1963.

47. A. Segura, L. Artús, R. Cuscó, T. Taniguchi, G. Cassabois, and B. Gil, "Natural optical anisotropy of h-bn: Highest giant birefringence in a bulk crystal through the mid-infrared to ultraviolet range," *Physical Review Materials*, vol. 2, no. 2, p. 024001, 2018.

48. B. Razavi and R. Behzad, *RF microelectronics*, vol. 2. Prentice Hall New Jersey, 1998.

49. T. Savas, M. Schattenburg, J. Carter, and H. I. Smith, "Large-area achromatic interferometric lithography for 100 nm period gratings and grids," *Journal of Vacuum Science & Technology B: Microelectronics and Nanometer Structures Processing, Measurement, and Phenomena*, vol. 14, no. 6, pp. 4167–4170, 1996.

62

50. K. Robbie, J. Sit, and M. Brett, "Advanced techniques for glancing angle deposition," *Journal of Vacuum Science & Technology B: Microelectronics and Nanometer Structures Processing, Measurement, and Phenomena*, vol. 16, no. 3, pp. 1115–1122, 1998.

51. K. Robbie and M. Brett, "Sculptured thin films and glancing angle deposition: Growth mechanics and applications," *Journal of Vacuum Science & Technology A: Vacuum, Surfaces, and Films*, vol. 15, no. 3, pp. 1460–1465, 1997.

52. K. Kimoto, Y. Kamiya, M. Nonoyama, and R. Uyeda, "An electron microscope study on fine metal particles prepared by evaporation in argon gas at low pressure," *Japanese journal of applied physics*, vol. 2, no. 11, p. 702, 1963.

53. M. M. Hawkeye and M. J. Brett, "Glancing angle deposition: fabrication, properties, and applications of micro-and nanostructured thin films," *Journal of Vacuum Science & Technology A: Vacuum, Surfaces, and Films*, vol. 25, no. 5, pp. 1317–1335, 2007.

54. J. A. Wollam, *Guide to Using WVASE Spectroscopic Ellipsometry Data Acquisition and Analysis Software.* J. A. Wollam Co. Inc, 1994.

55. M. Schubert, B. Rheinländer, J. A. Woollam, B. Johs, and C. M. Herzinger, "Extension of rotating-analyzer ellipsometry to generalized ellipsometry: determination of the dielectric function tensor from uniaxial tio 2," *JOSA A*, vol. 13, no. 4, pp. 875–883, 1996.

56. M. Schubert, "Generalized ellipsometry and complex optical systems," *Thin Solid Films*, vol. 313, pp. 323–332, 1998.

57. D. H. Goldstein, *Polarized Light, revised and expanded.* CRC press, 2003.

58. H. A. Lorentz, *The Theory of Electrons and Its Applications to the Phenomena of Light and Radiant Heat: A Course of Lectures Delivered in Columbia University, New York, in March and April, 1906*, vol. 29. Columbia University Press, 1909.

59. J. D. Jackson, *Classical electrodynamics.* John Wiley & Sons, 2012.

60. R. Biswas, E. Özbay, and K.-M. Ho, "Photonic band gaps with layer-by-layer double-etched structures," *Journal of applied physics*, vol. 80, no. 12, pp. 6749–6753, 1996.

REPORT DOCUMENTATION PAGE

1. REPORT DATE *(DD–MM–YYYY)*	2. REPORT TYPE	3. DATES COVERED *(From — To)*
21–03–2019	Master's Thesis	June 2017 — Mar 2019

4. TITLE AND SUBTITLE

Computational and Experimental Development of
2D Anisotropic Photonic Crystal Metamaterials

5a. CONTRACT NUMBER

5b. GRANT NUMBER

5c. PROGRAM ELEMENT NUMBER

6. AUTHOR(S)

Ethridge, James A

5d. PROJECT NUMBER

5e. TASK NUMBER

5f. WORK UNIT NUMBER

7. PERFORMING ORGANIZATION NAME(S) AND ADDRESS(ES)

Air Force Institute of Technology
Graduate School of Engineering and Management (AFIT/EN)
2950 Hobson Way
WPAFB OH 45433-7765

8. PERFORMING ORGANIZATION REPORT NUMBER

AFIT-ENP-19-MS-077

9. SPONSORING / MONITORING AGENCY NAME(S) AND ADDRESS(ES)

Air Force Office of Scientific Research
Arlington, VA 22203

10. SPONSOR/MONITOR'S ACRONYM(S)

AFOSR/RTB1

11. SPONSOR/MONITOR'S REPORT NUMBER(S)

12. DISTRIBUTION / AVAILABILITY STATEMENT

DISTRIBUTION STATEMENT A:
APPROVED FOR PUBLIC RELEASE; DISTRIBUTION UNLIMITED.

13. SUPPLEMENTARY NOTES

14. ABSTRACT

The future of optical devices involves manipulation of nanoscale structure in order to achieve full control over the properties of the device. To advance this further, novel samples that incorporate both photonic crystal (PhC) structure and metamaterial properties, known as PhC metamaterials, are proposed. These PhC metamaterials allow for complete control over the directionality of the light-matter interaction to serve in these new applications. To develop this technology, first, metamaterials with no PhC structure are fabricated using the technique of glancing angle deposition (GLAD) in the form of nanorod or nanohelical structures. These metamaterials are then characterized using Variable-Angle Spectral Ellipsometry (VASE) to extract their optical constants. Using these measured effective material parameters, a model for the corresponding metamaterial within a PC structure was developed in COMSOL Multiphysics to calculate the photonic bandgap (PBG) of that structure. Results show that a material with a complete and large PBG can be achieved with these PhC metamaterials.

15. SUBJECT TERMS

Photonic Crystals, Metamaterials, Bandgap, Ellipsometry, COMSOL

16. SECURITY CLASSIFICATION OF:			17. LIMITATION OF ABSTRACT	18. NUMBER OF PAGES	19a. NAME OF RESPONSIBLE PERSON
a. REPORT	b. ABSTRACT	c. THIS PAGE			Dr. Michael A. Marciniak, AFIT/ENP
U	U	U	UU	75	19b. TELEPHONE NUMBER *(include area code)* (937) 255-3636, x4529; Michael.Marciniak@afit.edu